UNCLASSIFIED

AD 256178

*Reproduced
by the*

ARMED SERVICES TECHNICAL INFORMATION AGENCY
ARLINGTON HALL STATION
ARLINGTON 12, VIRGINIA

DEPARTMENT OF DEFENSE
UNITED STATES OF AMERICA

UNCLASSIFIED

[redacted]

UNCLASSIFIED

AD256178

Total No. Pages: ii & 69

Copy No. ( ) of ( )

UNCLASSIFIED

...tion changed to
"HDD - WWRMDF-23
July 14, 1960. by amg.

PRESSURE DISTRIBUTION ON BLUNTED FLAT PLATES WITH SURFACE INCLINATION
(Title Unclassified)

DATA REPORT NO. 5134-5
TECHNICAL REPORT NO. 171

By A. Martellucci and A. Fields

Contract No. AF 33(616)-6692

Prepared for

Commander
Wright Air Development Division
Air Research and Development Command
Wright-Patterson Air Force Base, Ohio

Prepared by

General Applied Science Laboratories, Inc.
Merrick and Stewart Avenues
Westbury, L.I., New York

June 1960

Approved by:
Antonio Ferri
Technical Director

UNCLASSIFIED

[redacted]

[redacted]

TABLE OF CONTENTS

[redacted]

[redacted]

PRESSURE DISTRIBUTION ON BLUNTED FLAT PLATES WITH SURFACE INCLINATION

(Title Unclassified)

I INTRODUCTION

This report is presented as a partial fulfillment of the requirements of Air Force Contract No. AF 33(616)-6692 dated 25 May 1959.

The object of this report is to present and analyze the experimental surface pressures measured at a nominal Mach number of 8 on blunted flat plates. The tests are conducted in the B tunnel of the von Karman Gas Dynamics Facility, Arnold Engineering Development Center. Surface pressures and the heat transfer to the model were measured on two flat plates blunted by a semi-cylindrical leading edge. The nose radii of the two models are 0.10 and 0.50 inches. Both models had a chord length of 11.0 inches.

In this report the experimental pressure distributions are presented. The effects of angle of attack, Reynolds number and nose radius on the surface pressure distribution are considered. Tests were conducted over a range of 0° to 30° surface inclination. The free stream Reynolds number varied from 0.43×10^6 to 2.00×10^6 per foot. The heat transfer data will be published in a later report.

[redacted]

[redacted]

Several existing theories are presented and their comparisons with experimental data are made. Also presented are shadowgraphs of the flow about each model for several angles of attack.

[redacted]

[redacted]

II SYMBOLS

B	empirical $(1/2)^{2/3}$ or zero
b_δ	quantity defined by Equation 43
C_D	nose drag coefficient defined by Equation 47
d	nose cylinder diameter - inches
H	stagnation enthalpy - ft^2/sec^2
M	Mach number
P	pressure - lbs/ft^2
P_α	quantity defined by Equation 41
P_β	quantity defined by Equation 46
q	local velocity - ft/sec
r	nose radius - inches
Re	Reynolds number
R	gas constant - 1716 ft^2/sec^2 $^\circ$R; model nose radius, inches
S	entropy - ft^2/ sec^2; arc length measured from stagnation point, inches
T	temperature $^\circ$R
u, v	velocities defined in Figure 12
x	chordwise direction, inches
α	angle of attack - positive nose up
γ	ratio of specific heats

[redacted]

[redacted]

Δ	shock stand-off distance (see Figure 12)
ϵ	shock wave angle measured from free stream
θ	flow deviation measured from free stream
μ	Mach angle ($\sin^{-1} \frac{1}{M}$)
ρ	density - slugs/ft^3

Subscripts

∞	free stream conditions
0	free stream stagnation conditions
s_e	stagnation conditions behind a normal shock
δ	local conditions in the flow field outside the boundary layer
w	conditions at wall

[redacted]

[redacted]

III APPARATUS AND PROCEDURE

A. Tunnel

All tests were conducted in the Mach 8.0, 50 inch diameter continuous axisymmetric wind tunnel (Tunnel B) at the von Karman Gas Dynamics Facility, Arnold Engineering Development Center, Tullahoma, Tennessee. A complete description of this facility may be found in Reference 1.

B. Models

Both models were constructed of type number 304 stainless steel. The surface finish was nominally 50 microinches while the skin thickness was 0.25 inches. The nose radii of the two models are 0.10 inches and 0.50 inches, each model being 11.0 inches long. A photograph of the 0.50 inch radius model, before being positioned in the tunnel, is shown in Figure 1. The 0.10 inch radius model installed in the tunnel is shown in Figure 2. The model sting support and one cooling shoe can also be seen. Figure 3 shows the 0.50 inch radius model with the side and top plates removed so that the model instrumentation is visible.

Since the same models were used in the heat transfer tests, slots were milled longitudinally so that the skin thickness in the vicinity of the thermocouples was nominally 0.050 inches. The thermocouples were installed in these slots. A more thorough and comprehensive description of the heat transfer aspect of the models will be given in subsequent reports.

[redacted]

[redacted]

Static pressure tubes 1/16" O.D. with a 0.012" wall thickness were installed on the model. These orifices were placed in staggered rows to one side of the center line. Thermocouples were symmetrically placed in identical locations on the opposite side of the center line. The staggering technique was used to obtain a small axial placement of tubes. The location and number of the tubes used for each model is shown in Figures 4 and 5 and Tables 1 and 2 for the 0.10 inch radius and 0.50 inch radius models, respectively.

C. Test Conditions

All tests were conducted at a nominal stagnation temperature of 900°F. Three stagnation pressure levels, namely, 100 psia, 240 psia and 480 psia, were chosen to determine the effect of Reynolds number variation on the pressure and heat transfer results. Data obtained at the 100 psi level was inconsistent and therefore was not included in this report. The surface inclination of the plate varied from 0° to 30° in 2 1/2° increments. However, only representative angles of attack of 0°, 5°, 10°, 15°, 20° and 30° were chosen for this report.

The variations in test conditions influenced the tunnel boundary layer which in turn affected the tunnel Mach number. The test conditions are summarized below.

[redacted]

[redacted]

Model II(A)

P_o = 240 psi M = 8.03

P_o = 480 psi M = 8.03

Model II(B)

P_o = 240 psi M = 8.03

P_o = 480 psi M = 8.08

[redacted]

[redacted]

IV DISCUSSION OF EXPERIMENTAL RESULTS

All the pressure data used in this report are "preliminary unchecked data". Since preliminary data were used certain inconsistencies in the data arose and were unaccountable for. Therefore, questionable data were usually excluded from this report.

Because of the small nose radius on Model II(A), the nose region ($0 \leq x/d \leq 0.5$) was uninstrumented. Results of the pressure distribution on the nose region of Model II(B) are shown in Figures 6 through 11. Modified Newtonian plus Prandtl-Meyer pressure distribution closely approximates the experimental distribution.

In general, the data are self-consistent and comparison with several existing theories will subsequently be discussed in this report.

[redacted]

[redacted]

V THEORETICAL ANALYSES

A. Two-Dimensional Rotational Characteristics

The method of characteristics for supersonic rotational flow can be utilized to predict the flow field about blunted two-dimensional bodies. However, to begin the computation, properties in the region between the shock and body in the supersonic region must be known. Thus, the computation procedure that was utilized was divided into two categories:

1. Subsonic-Transonic Flow About a Circular Cylinder
2. 2-D Rotational Characteristics over an Arbitrary Body Blunted by a Circular Cylinder

A description of each category with the pertinent equations follows.

1. Subsonic-Transonic Region

The flow field about two-dimensional circular cylinders has been analyzed by several authors (Refs. 2, 3 and 4). In each method, the technique involved in computing the flow field is quite laborious and, consequently, time consuming. Since the object of this analysis is to define the properties in the transonic-supersonic region of the flow and not the details in the subsonic region, an approximate scheme was devised.

This method proceeds by assuming a shock shape. The relation defining the shock shape must be "even", hence, a shock of the following form was used (Figure 12)

$$r_s = r_b + \Delta + b_2^2\, \theta^2 + b_4\, \theta^4 \tag{1}$$

[redacted]

[redacted]

Since the shock wave radius in the vicinity of the stagnation region is known to be the best approximated by a concentric cylinder of radius $(r_b + \Delta)$, the square term must be eliminated. Therefore, a shock shape of the form

$$r_s = r_b + \Delta + b_4 \theta^4 \tag{2}$$

was used, where the parameter b_4 is to be determined from mass flow considerations. That is, equating the mass flow entering the shock (OA) to the mass flow passing through (AB) (Figure 12) provides the necessary cirterion to determine b_4.

Equating mass flow, and retaining only the linear terms in the derivatives one obtains:

$$\begin{aligned} \rho_\infty V_\infty Y_A = & \int_0^{\frac{1}{2}(\Delta + b_4\theta^4)} \left[\rho_B + \left(\frac{\partial \rho}{\partial r}\right)_A (r_A - r)\right] \left[u_A + \left(\frac{\partial u}{\partial r}\right)_A (r_A - r)\right] dr \; + \\ & + \int_{\frac{1}{2}(\Delta + b_4\theta^4)}^{\Delta + b_4\theta^4} \left[\rho_A + \left(\frac{\partial \rho}{\partial r}\right)_A (r_A - r)\right] \left[u_A + \left(\frac{\partial u}{\partial r}\right)_A (r_A - r)\right] dr \end{aligned} \tag{3}$$

Since the quantity b_4 can be expected to be small, only linear terms in b_4 were retained throughout the entire analysis. The pressure at point B was obtained from Newtonian flow. The velocity u, and density ρ were then obtained from compressible flow relations.

From Crocco's theorem,

$$\frac{a^2}{\gamma R} \text{ Grad } S = \text{Curl } V \times V \tag{4}$$

[redacted]

[redacted]

expanded in cylindrical coordinates one obtains

$$\frac{a^2}{\gamma R}\frac{\partial S}{\partial r} = -u\left(\frac{u}{r} + \frac{\partial u}{\partial r} - \frac{1}{r}\frac{\partial v}{\partial \theta}\right) \qquad (5)$$

But at the body

$$\frac{\partial S}{\partial r} = 0 \text{ and } \frac{1}{r}\frac{\partial v}{\partial \theta} = 0$$

hence

$$\left(\frac{\partial u}{\partial r}\right)_B = -\left(\frac{u}{r}\right)_B \qquad (6)$$

Differentiating the relation

$$\rho = \rho_{s_e}\left[1 - \left(\frac{V}{V_L}\right)^2\right]^{\frac{1}{\gamma - 1}} \qquad (7)$$

in the r direction, one obtains $\left(\frac{\partial \rho}{\partial r}\right)_B$ expressed in terms of $\left(\frac{\partial u}{\partial r}\right)_B$. Hence the first integral of Equation (3) can be evaluated in terms of b_4.

Defining

$$\beta = \tan^{-1}\left\{\frac{1}{r_s}\frac{d\,r_s}{d\,\theta}\right\} = \tan^{-1}\left\{\frac{4\,b_4\,\theta^3}{r_B + \Delta + b_4\,\theta^4}\right\} \qquad (8)$$

which when simplified can be written as

$$\beta = \beta_1 b_4 \qquad (9)$$

where

$$\beta_1 = \frac{4\,\theta^3}{r_B + \Delta}$$

In order to evaluate the second integral of Equation (3), the velocity and density and their derivatives immediately behind the shock must be determined, as a function of b_4. Within the approximation considered, the

[redacted]

[redacted]

velocity components behind the shock can now be expressed in the following form:

$$u = u_o + b_4 u_1 \qquad (10)$$

$$v = v_o + b_4 v_1 \qquad (11)$$

$$\rho = \rho_o + b_4 \rho_1 \qquad (12)$$

where

$$u_o = U_\infty \mathrm{Sin}\ \theta$$

$$u_1 = \frac{\beta_1}{(\gamma+1)U_\infty}\left[\cos\theta\left\{2U_\infty^2 \mathrm{Sin}_\theta^2 - \frac{1}{\cos^2\theta}\left[\gamma U_\infty^2 + U_\infty^2 \cos 2\theta - (\gamma-1)\right]\right\} - 2U_\infty^2 \mathrm{Sin}\ \theta\ \mathrm{Sin}\ 2\theta\right]$$

$$v_o = \frac{1}{(\gamma+1)U_\infty}\left[\mathrm{Sin}\ \theta \tan\theta\left\{\gamma U_\infty^2 + U_\infty^2 \cos 2\theta - (\gamma-1)\right\} - \cos\theta\left\{(\gamma-1) + 2U_\infty^2 \mathrm{Sin}^2\theta\right\}\right]$$

$$v_1 = \frac{\beta_1}{(\gamma+1)U_\infty}\left[\mathrm{Sin}\ \theta\left\{2U_\infty^2 \mathrm{Sin}^2\theta - \frac{1}{\cos^2\theta}\left(\gamma U_\infty^2 + U_\infty^2 \cos 2\theta - \gamma + 1\right)\right\} + 2U_\infty^2 \cos\theta\ \mathrm{Sin}\ 2\theta\right]$$

$$\rho_o = \left[\frac{(\gamma+1) M_\infty^2 \cos^2\theta}{(\gamma-1) M_\infty^2 \cos^2\theta + 2}\right]\rho_\infty$$

$$\rho_1 = \frac{2(\gamma+1) M_\infty^2 \beta_1 \mathrm{Sin}\ 2\theta}{\left[(\gamma-1)M_\infty^2 \cos^2\theta + 2\right]^2}\rho_\infty$$

and

$$U_\infty \equiv V_\infty / V_L$$

[redacted]

In addition, the entropy immediately behind the shock (Point A, Figure 12) can be expressed as

$$(\gamma-1)\frac{\Delta S}{R} = (\gamma-1)\frac{\Delta S_o}{R} + b_4(\gamma-1)\frac{\Delta S_1}{R} \tag{13}$$

where

$$(\gamma-1)\frac{\Delta S_o}{R} = \log_e\left[\frac{2\gamma M_\infty^2 \operatorname{Cos}^2\theta-(\gamma-1)}{\gamma+1}\right] - \gamma\log_e\left[\frac{(\gamma+1)M_\infty^2\operatorname{Cos}^2\theta}{(\gamma-1)M_\infty^2\operatorname{Cos}^2\theta+2}\right]$$

and

$$(\gamma-1)\frac{\Delta S_1}{R} = \beta_1 \operatorname{Sin}2\theta\left[\frac{2\gamma M_\infty^2}{2\gamma M_\infty^2\operatorname{Cos}^2\theta-(\gamma-1)} + \frac{\gamma(\gamma-1)M_\infty^2}{(\gamma-1)M_\infty^2\operatorname{Cos}^2\theta+2} - \frac{\gamma}{\operatorname{Cos}^2\theta}\right]$$

From Equations (10), (11) and (12) the derivatives with respect to θ of the following quantities; u, v and $\frac{\Delta S}{R}$, can be obtained in the form

$$\frac{d\phi_1}{d\theta} = \frac{d\phi_o}{d\theta} + b_4\frac{d\phi_1}{d\theta} \tag{14}$$

With the system of equations

[redacted]

$$\left.\begin{aligned}
&(1-\frac{u^2}{a^2})\frac{1}{r}\frac{\partial u}{\partial\theta}+(1-\frac{v^2}{\upsilon^2})\frac{\partial v}{\partial r}+\frac{v}{r}-\frac{uv}{a^2}(\frac{1}{r}\frac{\partial v}{\partial\theta}+\frac{\partial u}{\partial r})=0\\
&\frac{a^2}{\gamma R}\frac{\partial S}{\partial r}=-u(\frac{u}{r}+\frac{\partial u}{\partial r}-\frac{1}{r}\frac{\partial v}{\partial\theta})\\
&\frac{a^2}{\partial R}\frac{\partial S}{\partial\theta}=v(\frac{u}{r}+\frac{\partial u}{\partial r}-\frac{1}{r}\frac{\partial v}{\partial\theta})\\
&\frac{ds}{d\theta}=\frac{\partial S}{d\theta}+\frac{\partial S}{\partial r}\frac{dr}{d\theta}\\
&\frac{du}{d\theta}=\frac{\partial u}{\partial\theta}+\frac{\partial u}{\partial r}\frac{dr}{d\theta}\\
&\frac{dv}{d\theta}=\frac{\partial v}{\partial\theta}+\frac{\partial v}{\partial r}\frac{dr}{d\theta}
\end{aligned}\right\}\qquad(15)$$

The six unknowns

$$\frac{\partial u}{\partial\theta},\ \frac{\partial u}{\partial r},\ \frac{\partial v}{\partial\theta},\ \frac{\partial v}{\partial r},\ \frac{\partial S}{\partial\theta},\ \frac{\partial S}{\partial r}$$

can be determined.

The remaining term to be evaluated, $\frac{\partial\rho}{\partial r}$, can be obtained from the continuity relation

$$\frac{1}{r}\frac{\partial}{\partial\theta}(\rho u)+\frac{\partial}{\partial r}(\rho v)=0\qquad(16)$$

That is,

$$\frac{\partial\rho}{\partial r}=-\left[\frac{\rho}{rv}\frac{\partial u}{\partial\theta}+\frac{\rho}{v}\frac{\partial v}{\partial r}+\frac{u}{rv}\frac{\partial\rho}{\partial\theta}\right]\qquad(17)$$

[redacted]

where every term in the square bracket is known at the shock, in terms of b_4.

The second integral of Equation (3) can now be evaluated in terms of b_4. Hence, Equation (3) is now reduced to a linear algebraic equation which will yield the value of b_4.

In order to perform the numerical computation, it is necessary to know the shock detachment distance Δ. The results of the constant density solution (References 2, 5 and 6) yield detachment distances which are approximately 55% too small at Mach 3 and 45% too small at Mach 5. The first order solution of Whitham (Reference 2) is given by

$$\eta_b \equiv \frac{r_b}{r_s} = 1 - \frac{1}{2\lambda} \log_e \frac{4\lambda}{3} \tag{18}$$

and $\lambda = \rho_2/\rho_1 - 1$

or more exactly η_b is the value of η for which the following equation is satisfied

$$0 = \left[(\lambda + 1) K_1(\lambda) - \lambda K_1'(\lambda)\right] \frac{I_1(\lambda\eta)}{\eta} - \left[(\lambda + 1) I_1(\lambda) - \lambda I_1'(\lambda)\right] \frac{K_1(\lambda\eta)}{\eta} \tag{19}$$

I_1 and K_1 are modified Bessel functions of the first and second kind, respectively. I_1' and K_1' are their derivatives,

$$\begin{aligned} I_1(\lambda) &= \frac{1}{2}\left[I_0(\lambda) + I_2(\lambda)\right] \\ K_1(\lambda) &= -\frac{1}{2}\left[K_0(\lambda) + K_2(\lambda)\right] \end{aligned} \tag{20}$$

[redacted]

The results of the numerical solution of Belotserkovskii (Reference 3) are compared to the first order solution of Whitham (Reference 2) in the table below:

	Belotserkovskii (Ref. 3)	Whitham (Ref. 2)
M = 3	Δ/r_b = 0.703	Δ/r_b = 0.305
M = 4	= 0.546	= 0.279
M = 5	= 0.481	= 0.265

In order to find the shock detachment distance at Mach 8.00, the first order solution and the "exact" solution of Reference 2 (Eqs. 18 and 19) were solved and the results were Δ/r_b = 0.234 and 0.279, respectively. These results were obviously too small. To determine the detachment distance, since data at M = 8.0 was not available in literature, Equation (18) was used as a curve fit for Belotserkovskii's data. That is

$$\eta_b = 1 - \frac{1}{2(\lambda_o + \Delta\lambda)} \log_e \frac{4}{3}(\lambda_o + \Delta\lambda) \qquad (21)$$

where

$$\lambda_o = \left(\frac{\rho_2}{\rho_1}\right)_{M=5.00} - 1 = 4.000$$

$$\Delta\lambda = (\lambda)_{M=8.00} - (\lambda)_{M=5.00} = 0.565$$

[redacted]

[redacted]

The value for the detachment distance, Δ, determined from the above relation is

$$\Delta / r_b = 0.422$$

The corresponding value of b_4 obtained from Equation (3) is

$$b_4 = 0.1815$$

Thus the shock shape is defined as

$$\frac{r_s}{r_b} = 1.422 + 0.1815\, \theta^4 \tag{22}$$

and at $\theta = 55^\circ$

$$\frac{r_s}{r_b} = 1.576$$

With the shock specified, the velocities u and v and the entropy S/R and their derivatives in the r direction are known at the body and at the shock. To obtain data in the region between the shock and the body, a third order equation was used. In each case, the four boundary conditions were used to solve for the four coefficients. Hence along the line, $\theta = 55^\circ$, the following properties were determined at several points:

$$x/r_b,\ y/r_b,\ S/R,\ P/P_\infty,\ \theta,\ \mu$$

These data are the input to the characteristics analysis.

2. Two-Dimensional Rotational Characteristics

The analysis of the flow over blunted two-dimensional bodies has been computed by the method of characteristics for a rotational flow.

[redacted]

[redacted]

The equation of motion, when the total enthalpy H_0 is constant in the flow, can be expressed along the characteristic lines in the following form

$$\frac{1}{\gamma} \frac{dP}{P} + \frac{d\theta}{\sin\mu \cos\mu} = 0 \tag{23}$$

along the characteristic line

$$\tan(\theta + \mu) = \frac{dy}{dx} \tag{24}$$

and
$$\frac{1}{\gamma} \frac{dP}{P} - \frac{d\theta}{\sin\mu \cos\mu} = 0 \tag{25}$$

along the line

$$\tan(\theta - \mu) = \frac{dy}{dx} \tag{26}$$

and

$$dS = 0 \tag{27}$$

along the streamline defined by

$$\frac{dy}{dx} = \tan\theta \tag{28}$$

If the velocity vector, total enthalpy, and entropy are known at two points A and B (see sketch), the position of a point C at the intersection of the tangents AC to the characteristic line of the first family from A and the tangent BC to the characteristic line of the second family from B can be obtained since the value of μ can be calculated at A and B.

Assuming that the tangents AC and BC can be substituted for the characteristic lines between AC and BC, the first approximation to the

[redacted]

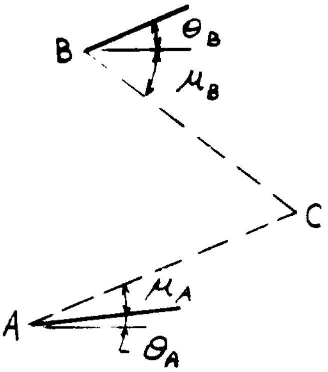

variation of flow properties between A and C and B and C can be obtained from Equations (23) and (25) by assuming that the coefficients are constant and equal to the corresponding values at A and B. However, the variation of the entropy along the characteristic lines must be known in order to determine P and θ at point C.

The assumption that the entropy is a continuous function in the region of the flow between the streamlines that pass through A and B, plus the fact that the entropy remains constant along a streamline leads to the equations

$$(\Delta S)_{AC} = S_C - S_A \tag{28}$$

$$(\Delta S)_{BC} = S_C - S_B \tag{29}$$

and

$$S_C = S_A + \left(\frac{dS}{dn}\right)_{AC} (\Delta n)_{AC} = S_A + \left(\frac{dS}{dn}\right)_{AC} (x_C - x_A) \left[\frac{\sin \mu}{\text{Cos}\,(\theta + \mu)}\right]_A \tag{30}$$

$$S_C = S_B + \left(\frac{dS}{dn}\right)_{BC} (\Delta n)_{BC} = S_B - \left(\frac{dS}{dn}\right)_{BC} (x_C - x_B) \left[\frac{\sin \mu}{\text{Cos}(\theta - \mu)}\right]_B \tag{31}$$

where $\frac{ds}{dn}$ is the gradient normal to the streamlines, and Δn is the normal distance between the streamline at A or B and the streamline passing at C.

[redacted]

Therefore assuming that

$$\left(\frac{dS}{dn}\right)_{AC} = \left(\frac{dS}{dn}\right)_{BC} = \left(\frac{dS}{dn}\right)_{AB} \tag{32}$$

S_C can be determined once $\frac{dS}{dn}$ is obtained from the expression

$$\left(\frac{dS}{dn}\right)_{AB} = \frac{S_B - S_A}{\frac{x_C - x_A}{\left[\mathrm{Cos}(\theta + \mu)\right]_A} \ \mathrm{Sin}\ \mu_A \ \frac{x_C - x_B}{\left[\mathrm{Cos}(\theta - \mu)\right]_B}} \tag{33}$$

The pressure P_C and the flow deviation θ_C can then be obtained from the relations

$$P_C = \frac{\theta_A - \theta_B + \frac{1}{\gamma}\left[\mathrm{Sin}\ \mu_A \mathrm{Cos}\ \mu_A + \mathrm{Sin}\ \mu_B \ \mathrm{Cos}\ \mu_B\right]}{\frac{\mathrm{Sin}\ \mu_A \ \mathrm{Cos}\ \mu_A}{\gamma P_A} + \frac{\mathrm{Sin}\ \mu_B \mathrm{Cos}\ \mu_B}{\gamma P_B}} \tag{34}$$

$$\theta = \theta_A + \frac{1}{\gamma} \mathrm{Sin}\ \mu_A \ \mathrm{Cos}\ \mu_A \ \frac{P_A - P_C}{P_A} \tag{35}$$

Shock Conditions

The determination of points on the shock were obtained from the following shock relations,

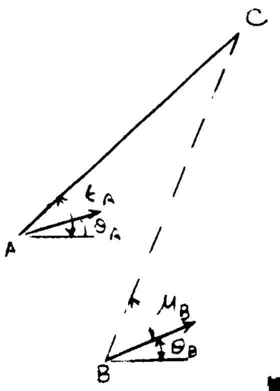

$$\frac{V_{n_C}}{V_\infty} = \frac{(\gamma - 1)M_\infty^2 \ \mathrm{Sin}^2\ \epsilon + 2}{(\gamma + 1)\ M_1^2 \ \mathrm{Sin}^{\ 2}\ \epsilon} \ \mathrm{Sin}\ \epsilon \tag{36}$$

$$\frac{V_{T_C}}{V_\infty} = \mathrm{Cos}\ \epsilon \tag{37}$$

$$V_{N_C}^{\ 2} + V_{T_C}^{\ 2} = V_C^{\ 2} \tag{38}$$

[redacted]

[redacted]

$$\frac{P_C}{P_\infty} = \frac{2\gamma M_\infty^2 \operatorname{Sin}^2 \epsilon - (\gamma - 1)}{(\gamma + 1)} \tag{39}$$

and the characteristic relation

$$\frac{1}{\gamma}\, \frac{P_A - P_C}{P_A} + \frac{\theta_A - \theta_C}{\operatorname{Sin}\mu_A \operatorname{Cos}\mu_A} = 0 \tag{40}$$

The conservation of tangential momentum across the shock can be expressed as

$$V_\infty = V \ \operatorname{Cos}\theta + \tan\epsilon \ \operatorname{Sin}\theta \tag{41}$$

The properties at point C (see sketch) on the shock must satisfy both the shock and characteristic equations. Since the problem was to be performed on an automatic computing machine, an iterative scheme on Equation (41) was decided upon as being the most expeditious way of obtaining a solution. The shock inclination, $\epsilon_o^{(1)}$, at C was selected and then $\epsilon_o^{(2)}$ was determined from Equation (41).

[redacted]

Boundary Conditions

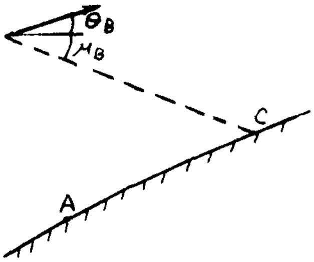

To determine properties on the body (e.g., Point C), the second family characteristic equation (Eq. 25) and the and the geometry of the body are used. Since the body is a streamline, $S_A = S_C$. The flow deviation is known for the geometry, thus one can solve Equation 25 directly for P. That is,

$$P_C = P_B \left[1 + \gamma \frac{\theta_B - \theta_C}{\sin \mu_B \cos \mu_B} \right] \qquad (42)$$

The above equations were programmed for the Bendix G-15 digital computer. In order to systematize the computations, the flow field was divided into three regions (Figure 13).

1. Region A is defined by the second family line from point S and the first family line from point B.

2. Region B is defined by the body and the second family line from point C.

3. Region C is the remaining flow field.

The computation in region C was performed along second family lines. In this manner, the program is able to sense terminal points of the body profile.

Attention is currently being devoted to minimizing the computer production time while retaining reliability. The problem is hampered solely due to the limited capacity of the computer availabile. However, modifications are being made which will substantially reduce the computer production time. Presented in this report are the characteristic analyses for two angles of attack, namely, $\alpha = 0^{\circ}$ and $\alpha = 5^{\circ}$. In a subsequent report several additional cases will be presented, including a displacement thickness analysis for which the inviscid two-dimensional characteristic will be computed.

B. Modified Newtonian Pressure Distribution

This method for predicting the pressure distribution on the surface of a blunted flat plate is discussed in detail in References 7 and 8. On the flat portion of a blunted plate, the normal to the free stream direction is equal to the compliment of the angle of incidence of the plate.

The equation relating the pressure to the plate incidence (Ref. 8) can be written as

$$P_{\alpha}/P_{s_e} = \mathrm{Sin}^2\alpha + \frac{P_{\infty}}{P_{s_e}} \mathrm{Cos}^2\alpha \tag{43}$$

For a given free stream Mach number, the pressure distribution is solely a function of surface inclination. Therefore on the constant inclination surface of the flat plate, the pressure as predicted by Newtonian theory is constant.

[redacted]

C. Modified Newtonian Plus Prandtl-Meyer Pressure Distribution

This method attempts to modify the body pressure distribution predicted by the Newtonian theory from the point on the body surface where the pressure and pressure gradient is equal to that predicted by Prandtl-Meyer flow. A more complete description of its use is given in Ref. 8.

The Prandtl-Meyer correction to Newtonian theory tends to alleviate somewhat the overexpansion that the modified Newtonian theory predicts.

D. Wedge Solution

This method is simply the solution to a pointed two-dimensional wedge inclined to the free stream at the same angle as the blunted flat plate. Theoretically, at a large distance downstream from the nose, the pressures predicted by the blunted flat plate and the wedge solution should be identical. For a given length flat plate, the wedge technique would obviously be more applicable for a smaller nose radius on the blunted plate.

E. Creager's Approximate Pressure Distribution for Blunted Flat Plates

This technique, as outlined more completely in References 9 and 10, assumes that:

1. A detached bow shock wave exists
2. The flow field is comprised of a viscous boundary layer adjacent to the surface of the body, plus an inviscid region

[redacted]

[redacted]

between the boundary layer and bow shock.

3. The displacement effect of the boundary layer perturbs the inviscid flow field.

If the above assumptions are valid then the perturbation may be expressed as:

$$\frac{P}{P_{\alpha\beta}} = 1 + \frac{b_\delta M_\delta^3 \chi}{\sqrt{Re_\delta}} \tag{44}$$

where

$$b_\delta = \left[\frac{0.865}{M_\delta^2} \; \frac{T_w}{T_\delta} + 0.166\,(\gamma - 1) \right] \gamma \tag{45}$$

From References 2, 3, 4, and 7 of Reference 9 it is further assumed that the inviscid pressure is given by a sum of two terms: one including a contribution due to the surface inclination and the second due to the shock wave shape.

Therefore it follows that

$$\frac{P_{\alpha\beta}}{P_\infty} = \frac{P_\alpha}{P_\infty} + \frac{P_\beta}{P_\infty} \tag{46}$$

Combining Equations (42) and (44) and multiplying both sides by P_∞ / P_{s_e}

$$\frac{P}{P_{s_e}} = \left[\frac{P_\alpha}{P_{s_e}} + \frac{P_\beta}{P_{s_e}} \right] + \left[1 + b_\delta\, M_\delta^3 / \sqrt{Re_\delta} \right] \tag{47}$$

The inviscid pressure terms (Eq. (46)) merit some further consideration: $\frac{P_\alpha}{P_\infty}$ is assumed to be a function of the surface inclination.

[redacted]

As mentioned in Reference 9, this term is assumed to be given by the modified Newtonian impact theory. However, as pointed out in Section VD of this report, the surface pressure should approach that value given by an equivalent wedge.

It is for these reasons that the chordwise pressure distributions as given by Reference 9, have been calculated by assuming a modified Newtonian distribution for the large nose radius model and an equivalent wedge value for the small nose radius model.

The second contribution to the inviscid surface pressure (that due to shock wave shape) has been computed by utilizing the blast-wave theory. From Reference 9 this is assumed to be given by:

$$\frac{P_\beta}{P_\infty} = BC_\gamma \left[\frac{C_D}{\frac{x+\Delta}{d}} \right]^{2/3} M_\infty^2 \tag{48}$$

where

$C_\gamma = 0.112$, and C_D is given by:

$$C_D = \frac{1}{\frac{\gamma}{2} P_\infty M_\infty^2 \frac{d}{2}} \int_0^x P \tan \theta_w dx \tag{49}$$

For the body at angle of attack, the inclination of the circular nose is:

$\theta_w = 90 - a$

Also

$x = r - r \cos a$

[redacted]

The limits of integration for Equation (47) have been modified in order to incorporate the portion of the nose which most influences the drag coefficient. Therefore C_D as suggested in Reference 9 was modified to:

$$C_D = \frac{1}{\frac{\gamma}{2} P_\infty M_\infty^2 \; r} \int_{r(1-\cos a)}^{r(1-\sin a)} P \tan \theta_w \, dx \qquad (50)$$

The contribution to the pressure for the zero angle of attack case of each term in Equation (45) can be seen in Figures 14 and 15 for each of the two models.

[redacted]

VI DISCUSSION OF RESULTS

The pressure distribution on two blunted flat plates were experimentally determined at a nominal Mach number of 8.0 for a 0° to 30° angle of attack range. Tests were conducted over a free stream Reynolds number range of 0.43×10^6 to 2.00×10^6 per foot. The two models were blunted by semicylindrical leading edges with nose radii of 0.10 inches and 0.50 inches. Both models had a chord length of 11.0 inches.

The experimental pressure distribution on the cylindrical nose of Model II(B) (1/2" r) has been plotted and compared to the modified Newtonian impact theory. The results are shown for several angles of attack, namely, 0°, 5°, 10°, 15°, 20° and 30°. It is generally concluded that the modified Newtonian theory is in good agreement with experiment in the nose region of blunt bodies (Ref. 6, page 257). One will note from the figures (6 to 11) that the agreement with experiment is not as good as can be expected. It appears that the model angle of attack is greater than the value indicated on the "Preliminary Data Sheets". For example, if the model angle of attack was 18° or 19° instead of 15° (Fig. 9), the modified Newtonian theory would be in good agreement with experiment.

The pressure distribution on the 1/2" nose radius flat plate model tends to approach the Newtonian value for all angles of attack (Figs. 16 to 21). In addition, for the low angle of attack range, blast theory plus the viscous correction (Refs. 9 and 10) accurately predicts the pressure variation on the flat plate. The agreement between the analysis of Reference 9 in the forward region of the flat plate is quite poor for larger angles of attack. The asymptotic solution for Creager's analysis for the 1/2"r model is the Newtonian value. Therefore, even for the larger angles of attack, the blast theory predicts reasonably well the pressures on the rearward portion of the plate. The rotational characteristics analysis has been computed for $\alpha = 0^{\circ}$ and 5° and the results agree well with experiment.

For the 0.10" nose radius model, the pressure distribution on the flat plate tends to approach the wedge value. Hence, the wedge value was used as the asymptotic solution in the analysis of Reference 9. The blast solution plus the viscous correction accurately predicts the pressure distribution on the flat plate over the entire angle of attack range considered (Figs. 22 to 27). For comparison, the zero blast solution ($B = 0$, Eq. (48)) is also shown. For higher angles of attack (20°-30°) this solution appears to be in slightly better agreement than the blast theory. This is to be expected, since the majority of streamlines that "wet" the body pass through the oblique portion of the bow shock. Hence the blunted flat plate acts more like a sharp wedge. Several shadowgraphs of each model are shown in Figures 28 to 39 for the entire angle of attack spectrum.

[redacted]

REFERENCES

1. "AEDC Test Facilities Handbook", Arnold Engineering Development Center, January 1959.

2. Whitham, G. B., "A Note on the Stand-Off Distance of the Shock in High Speed Flow Past a Circular Cylinder", Communications on Pure and Applied Mathematics, November 1957, pp. 531-535.

3. Belotserkovskii, O. M., "Flow Past a Circular Cylinder with a Detached Shock Wave", Doklady Akad Nank SSSR, Vol. 113, No. 3, 1957.

4. Uchida, S. and Yasuhara, M., "The Rotational Flow Field Behind a Curved Shock Wave Calculated by the Method of Flux Analysis" Journal of the Aeronautical Sciences, Vol. 23, No. 9, September 1956, pp. 830-845.

5. Hayes, W. D. and Probstein, R. F., "Hypersonic Flow Theory", Academic Press, New York, 1959, pp. 152 ff, 224.

6. Truitt, R. W., "Hypersonic Aerodynamics", The Ronald Press Co., New York, 1959, pp. 241 ff.

7. Lees, Lester, "Hypersonic Flow", Institute of the Aeronautical Sciences Preprint No. 554, 1955.

8. Aerodynamics Department, "Pressure Distribution on a Blunted 15° Circular Cone", GASL Technical Report No. 136 (Data Report No. 5134-1, February 1960.

9. Creager, M. O., "Effects of Leading-Edge Blunting on the Local Heat Transfer and Pressure Distributions Over Flat Plates in Supersonic Flow", NACA TN 4142, 1957.

10. Creager, M. O., "The Effect of Leading-Edge Sweep and Surface Inclination on the Hypersonic Flow Field Over a Blunt Flat Plate", NASA Memo 12-26-58A, 1959.

[redacted]

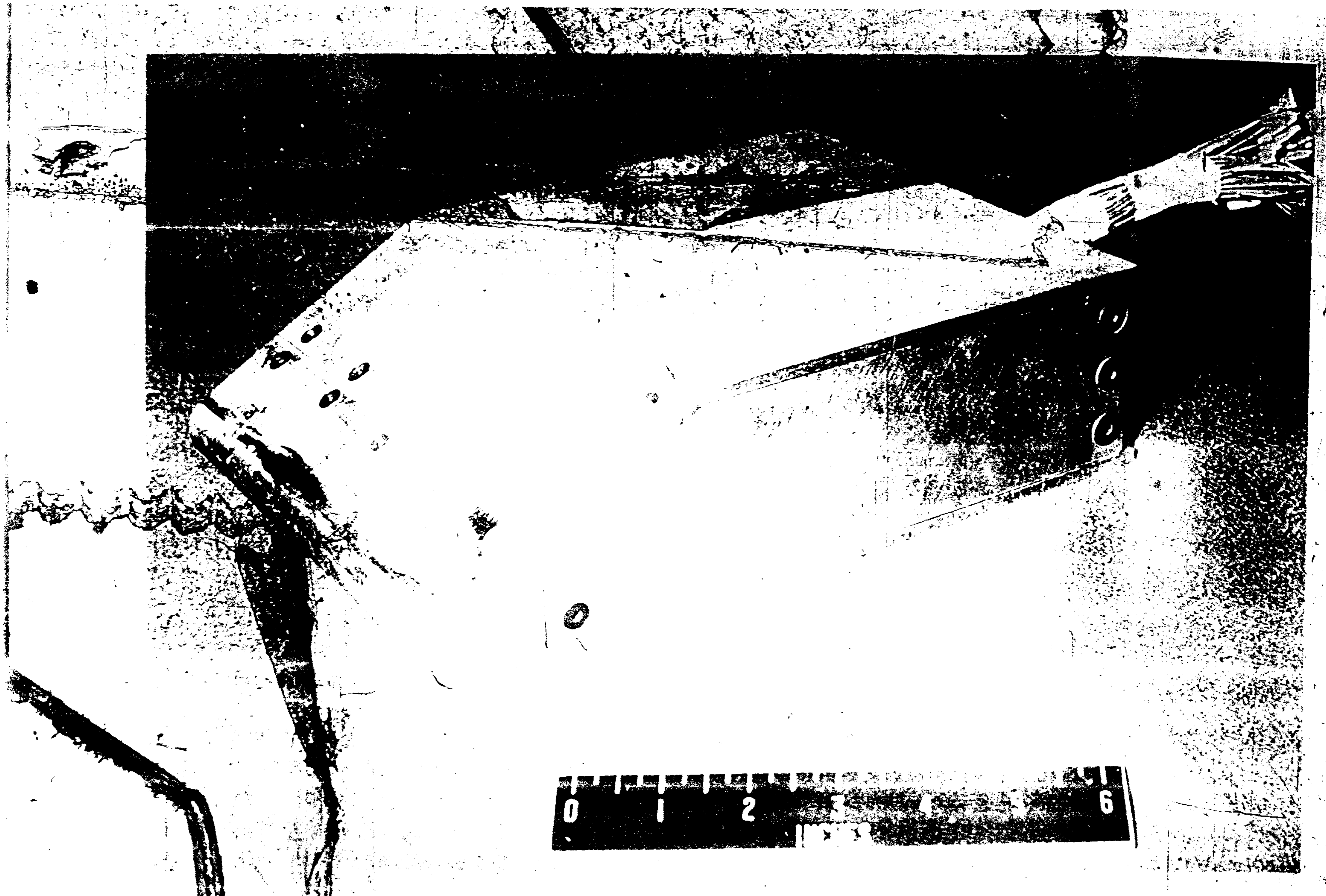

Figure 1 - 0.50 Inch Nose Flat Plate Model

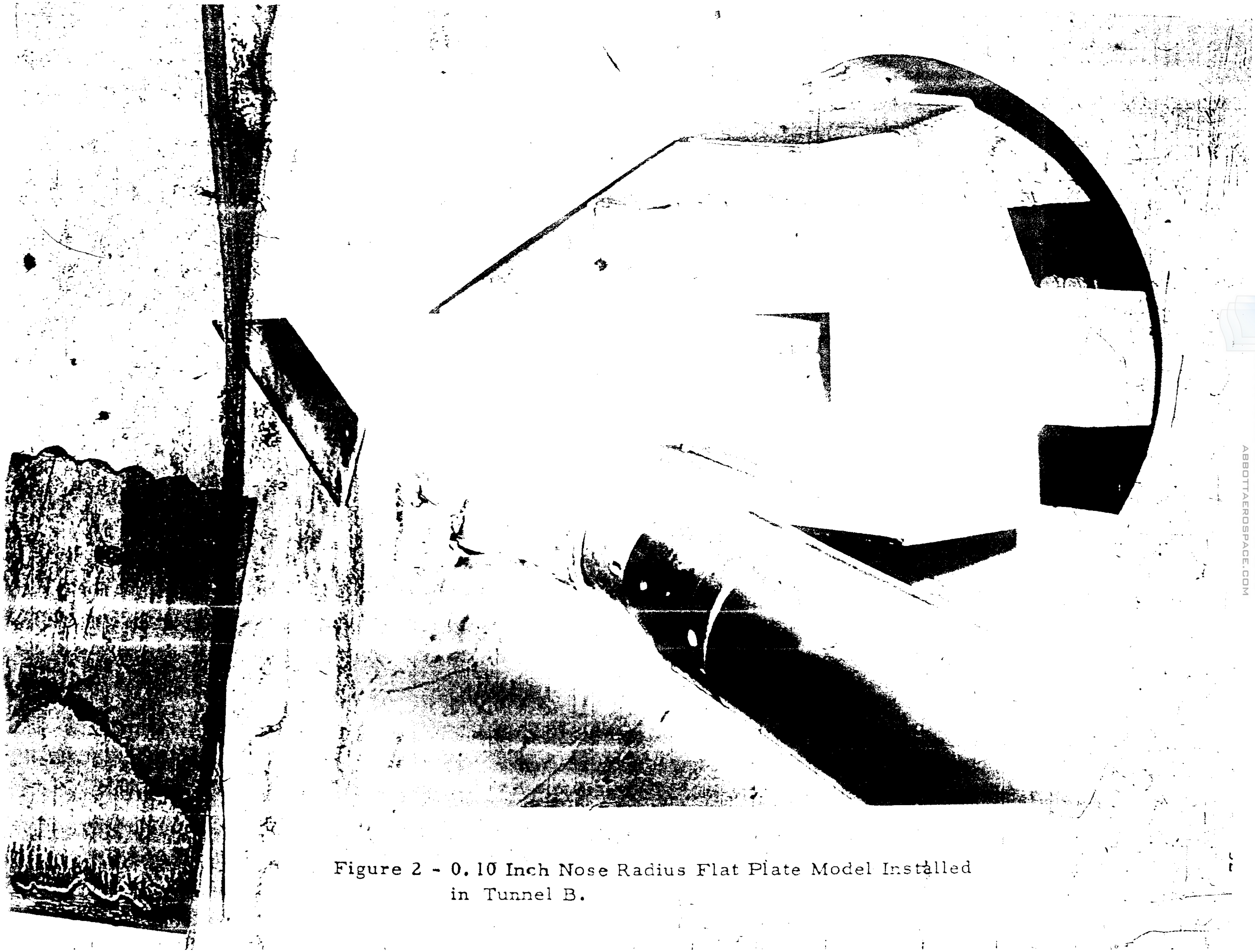

Figure 2 - 0.10 Inch Nose Radius Flat Plate Model Installed in Tunnel B.

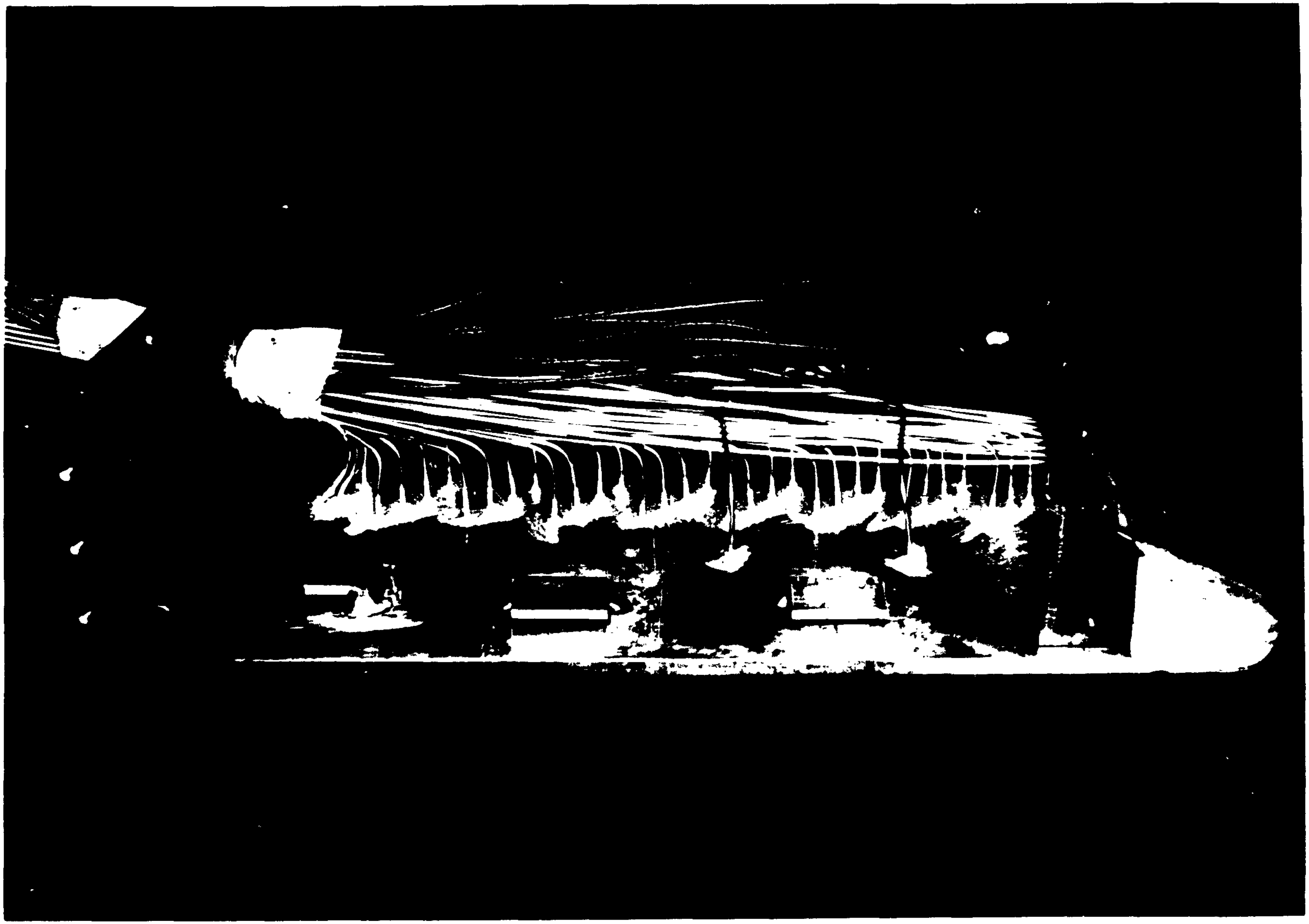

Figure 3 - 0.50 Inch Nose Radius Flat Plate Model Instrumentation

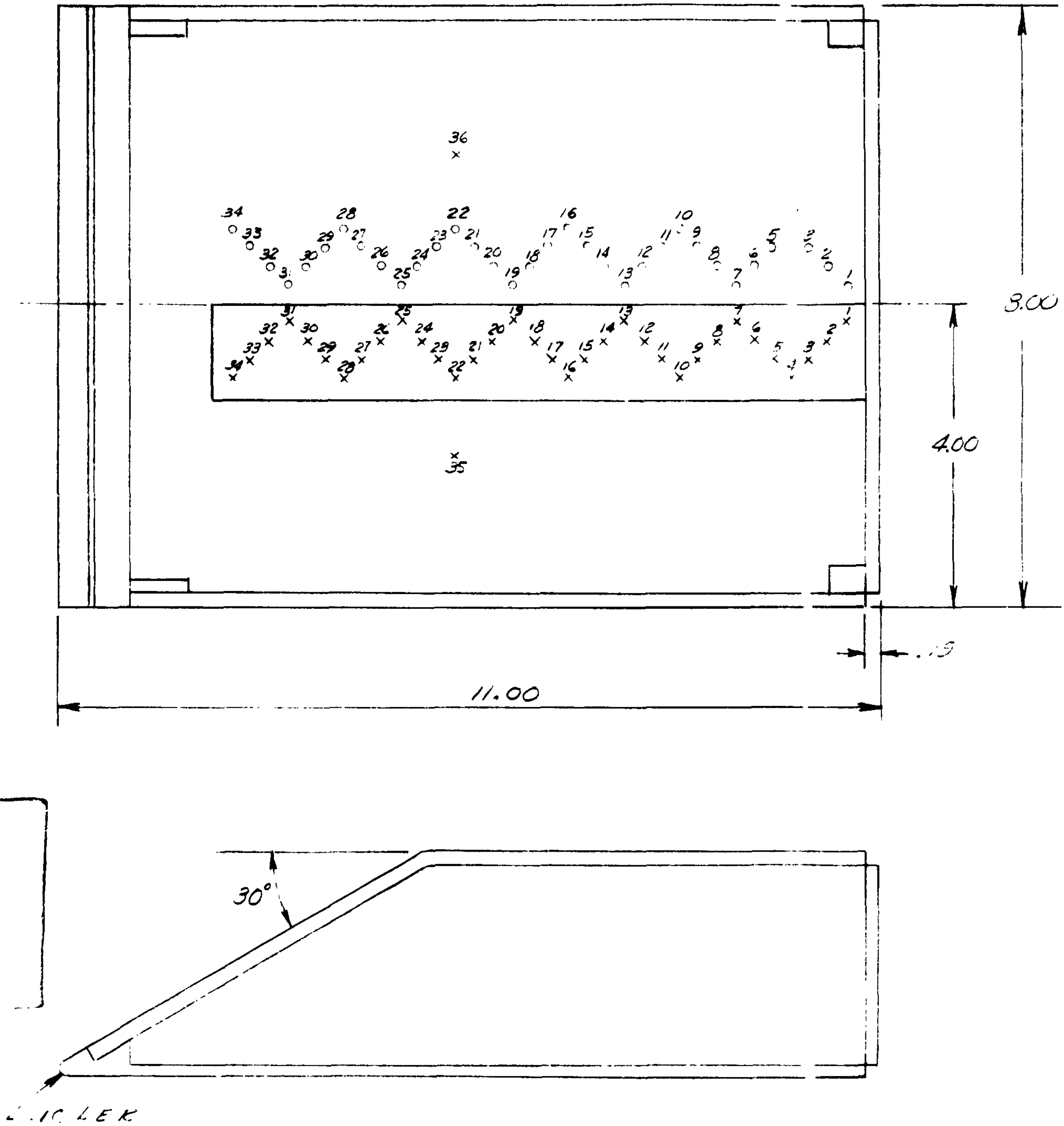

1

FIG. 4

TAP LOCATIONS FOR II-A ASSEMBLY

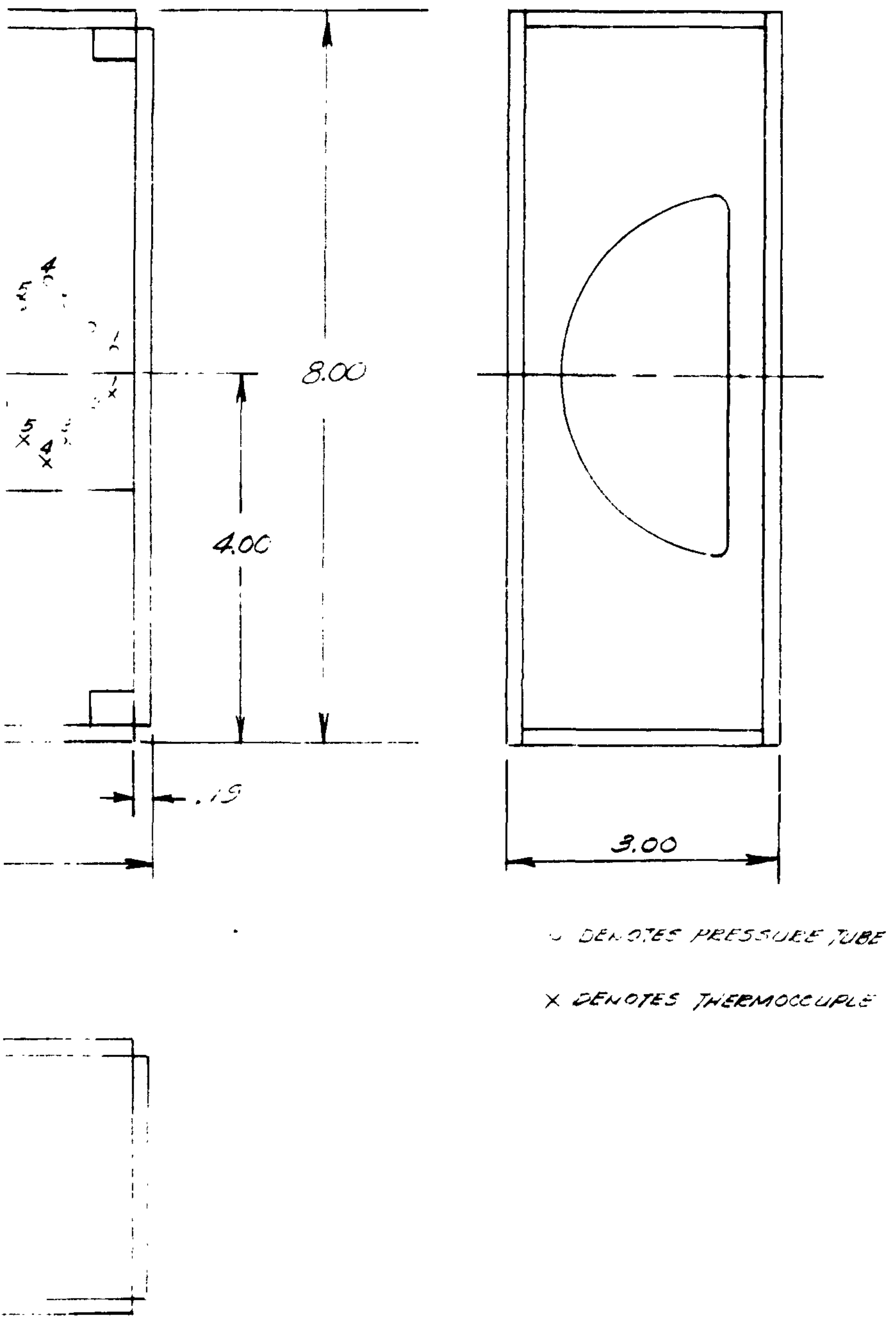

○ DENOTES PRESSURE TUBE

× DENOTES THERMOCOUPLE

2

-4 ASSEMBLY

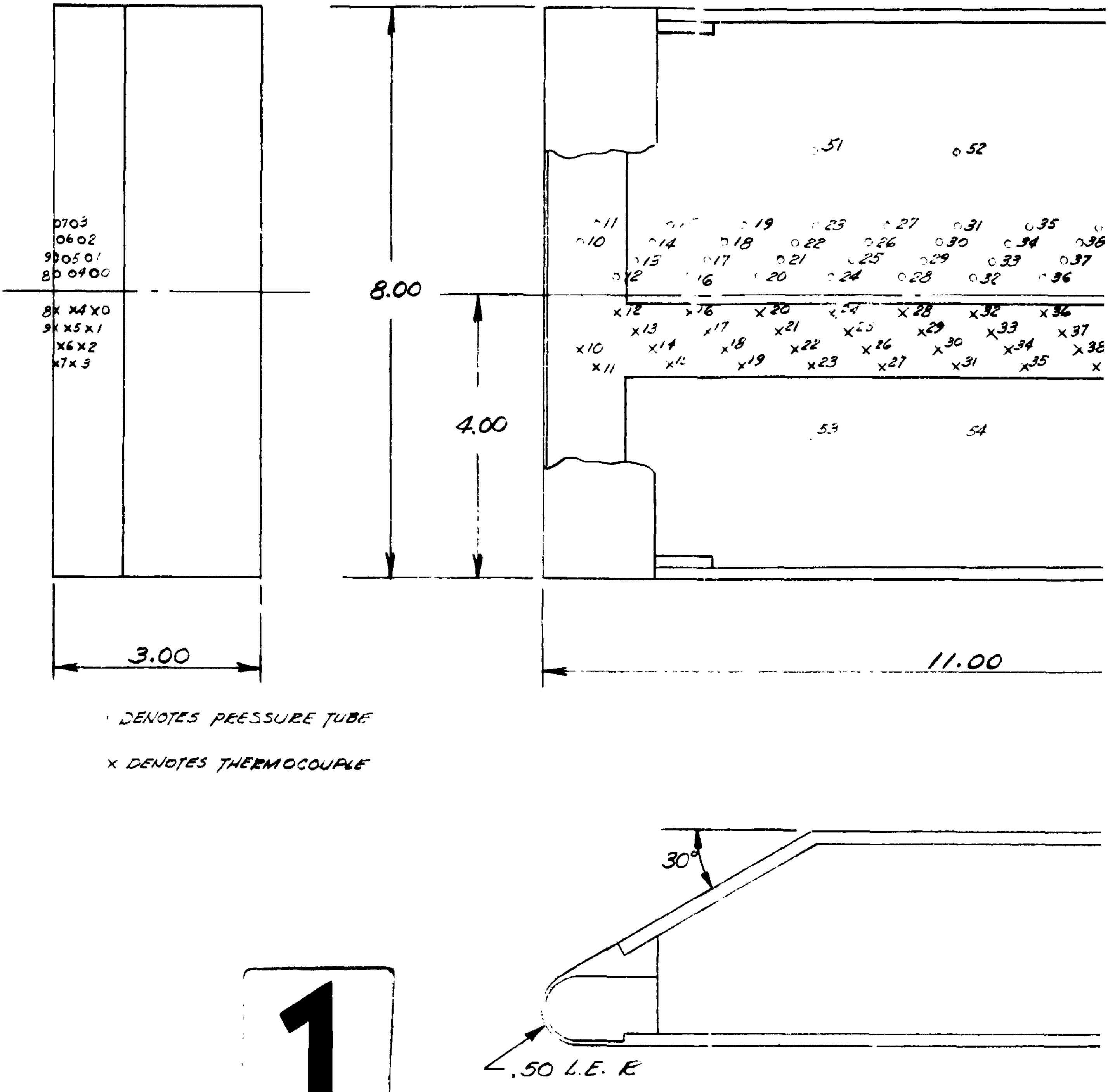

○ DENOTES PRESSURE TUBE

x DENOTES THERMOCOUPLE

1

FIG. 5
TAP LOCATIONS FOR II-B ASSEMBLY

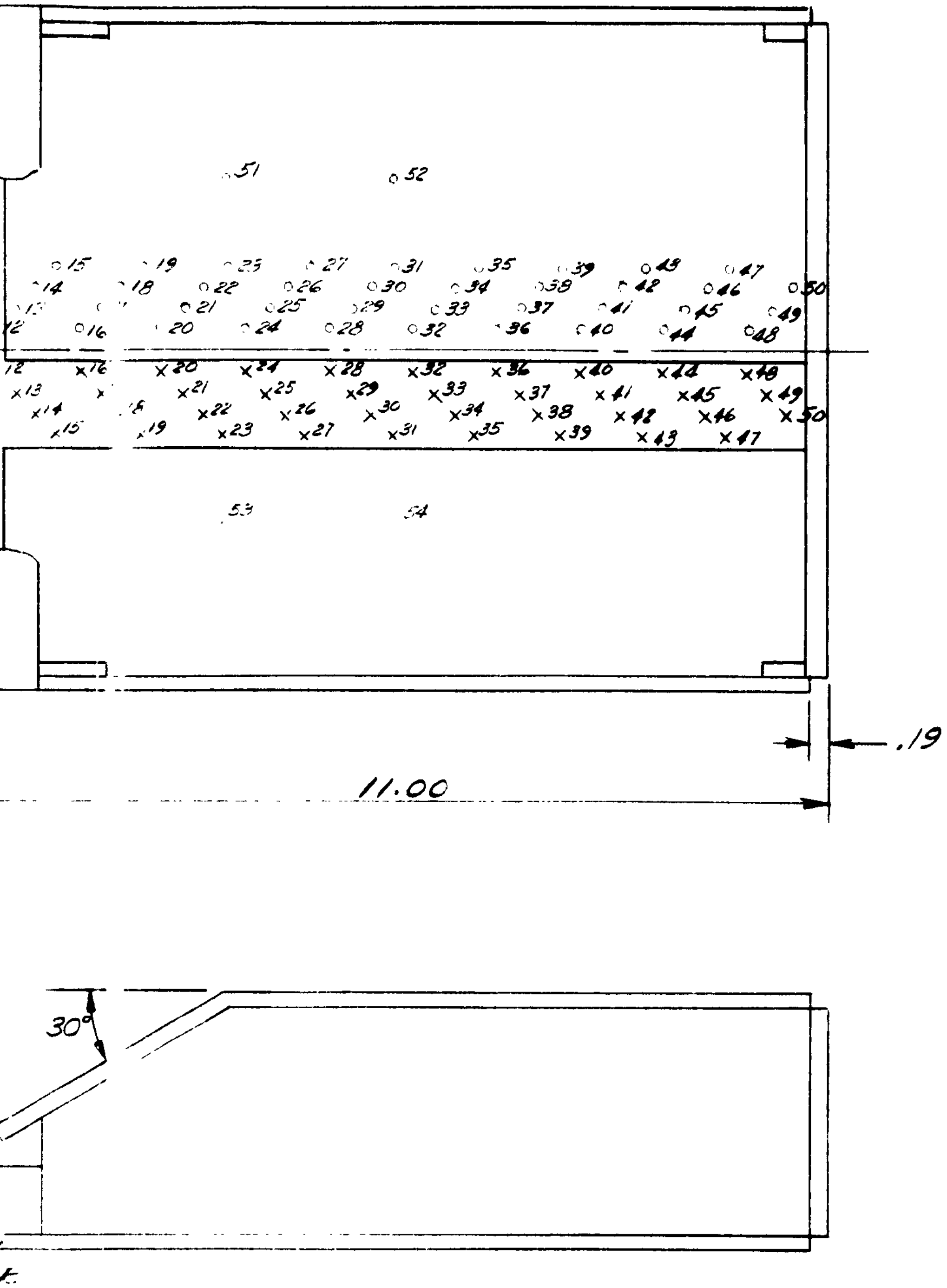

2

FIG. 5
FOR II-B ASSEMBLY

[redacted]

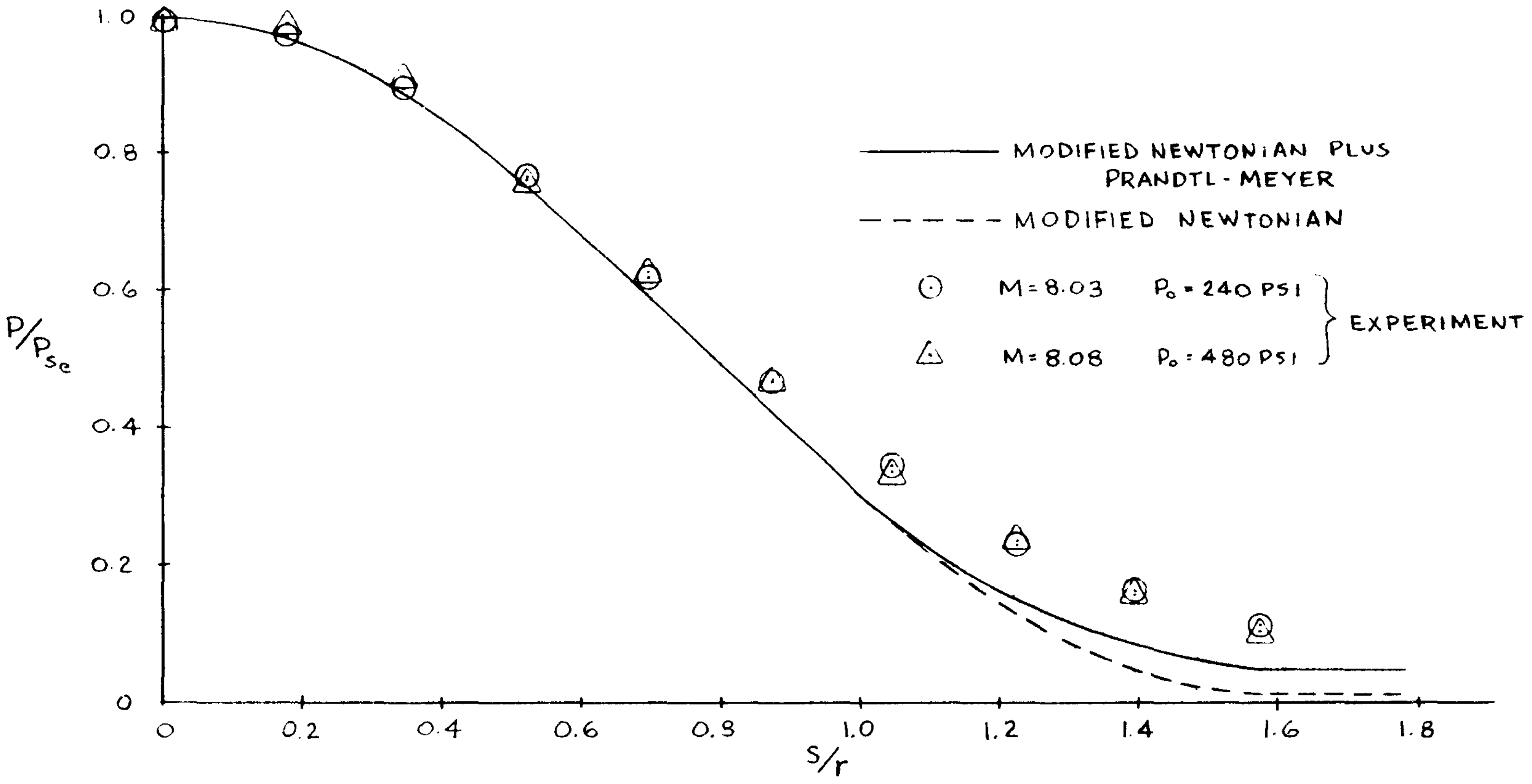

Figure 6 - Pressure Distribution on the Nose Cylinder of the 0.50 Inch Nose Radius Flat Plate Model - $\alpha = 0^{\circ}$

[redacted]

[redacted]

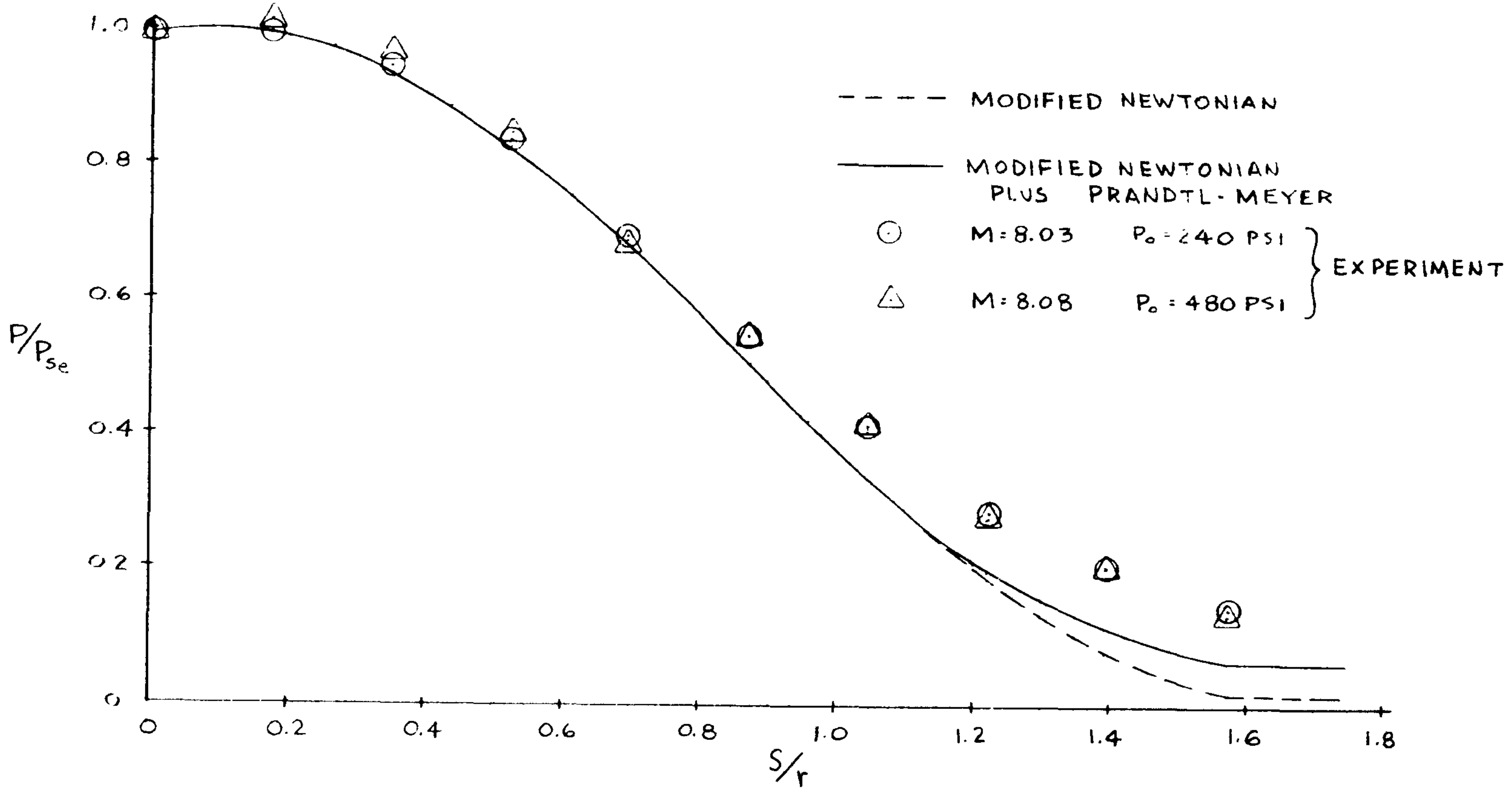

Figure 7 - Pressure Distribution on the Nose Cylinder of the 0.50 Inch Nose Radius Flat Plate Model - $\alpha = 5^{o}$

[redacted]

[redacted]

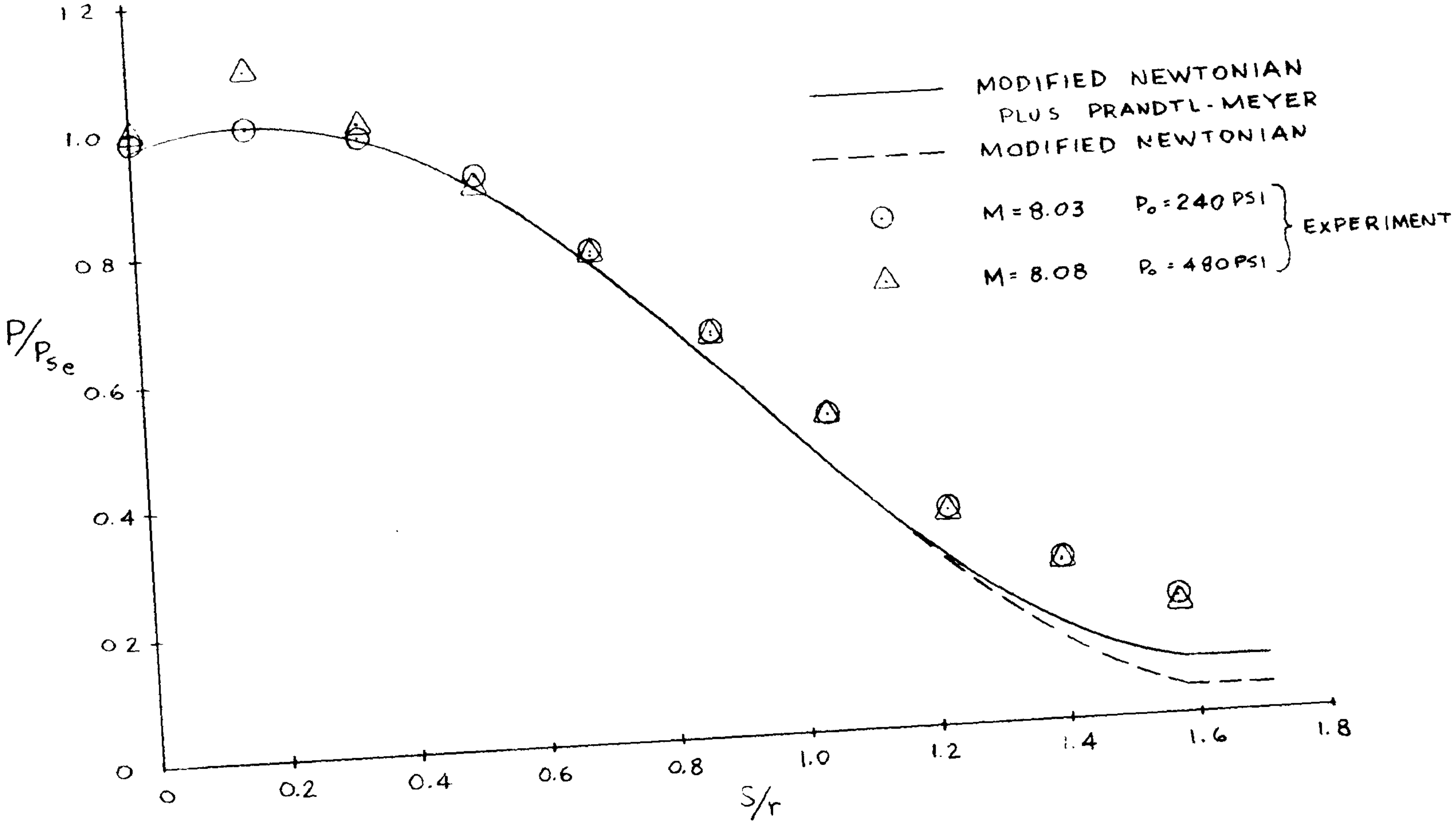

Figure 8 - Pressure Distribution on the Nose Cylinder of the 0.50 Inch Nose Radius Flat Plate Model - $\alpha = 10^{o}$

[redacted]

[redacted]

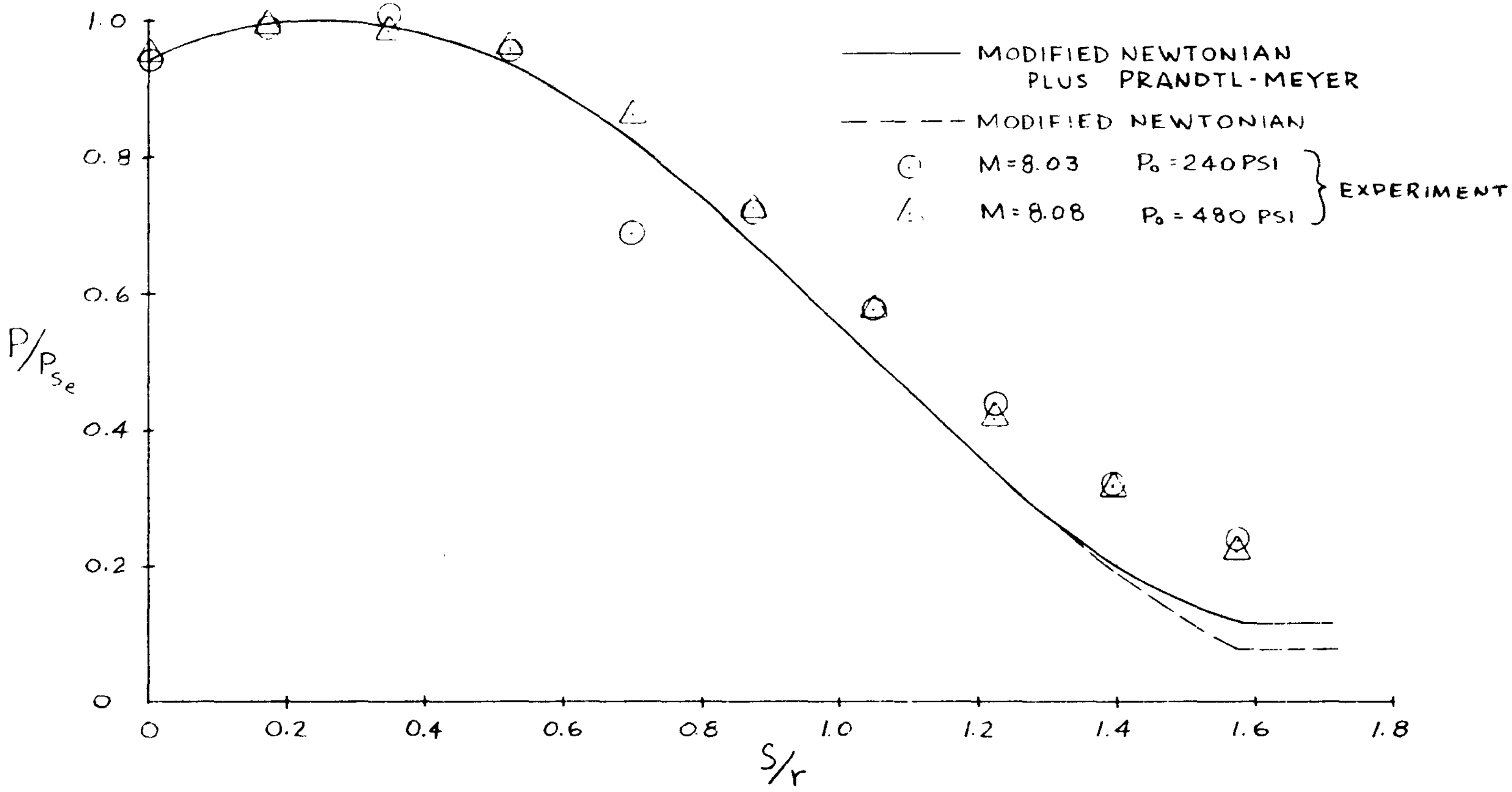

Figure 9 - Pressure Distribution on the Nose Cylinder of the 0.50 Inch Nose Radius Flat Plate Model - α = 15°

[redacted]

[redacted]

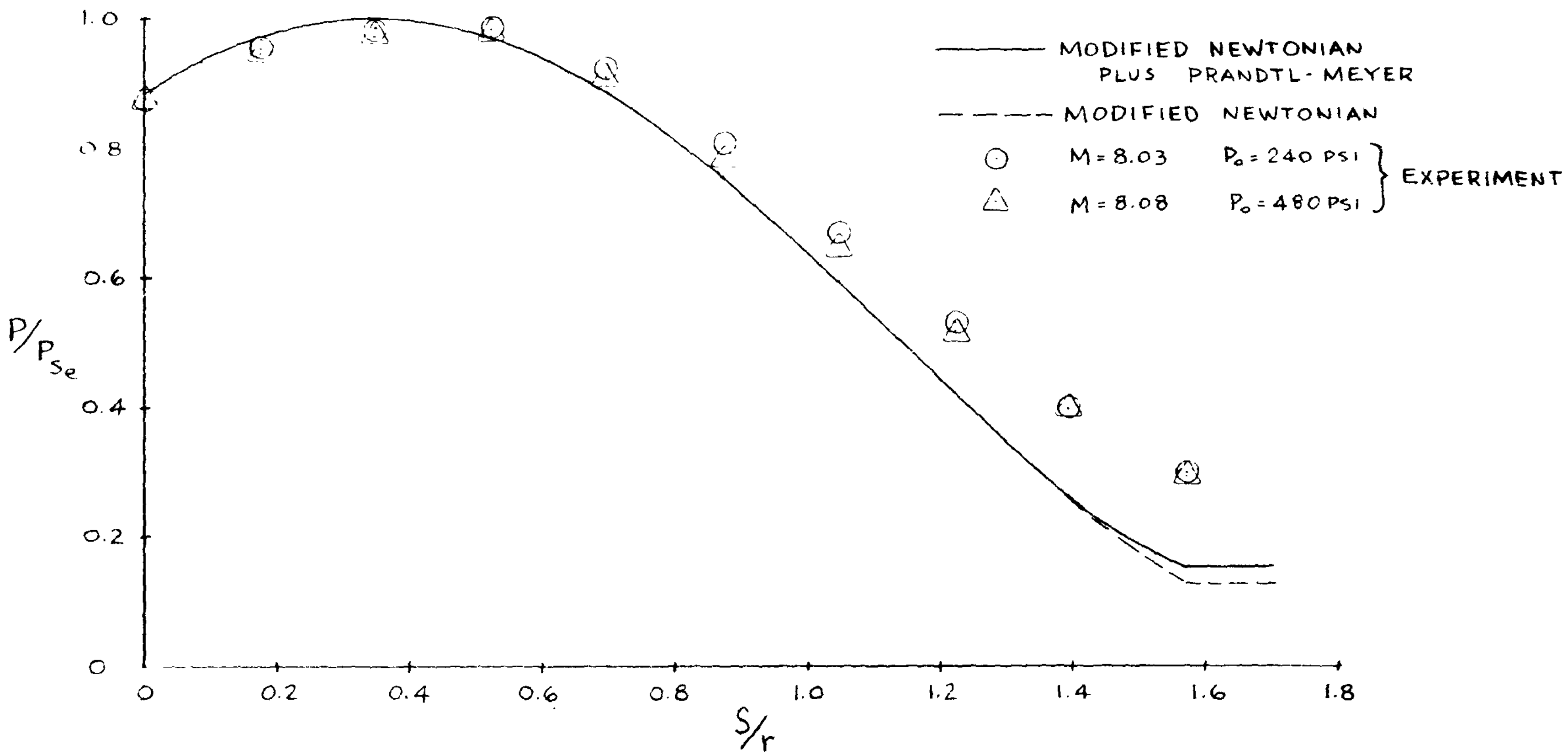

Figure 10 - Pressure Distribution on the Nose Cylinder of the 0.50 Inch Nose Radius Flat Plate Model - α = 20°

[redacted]

[redacted]

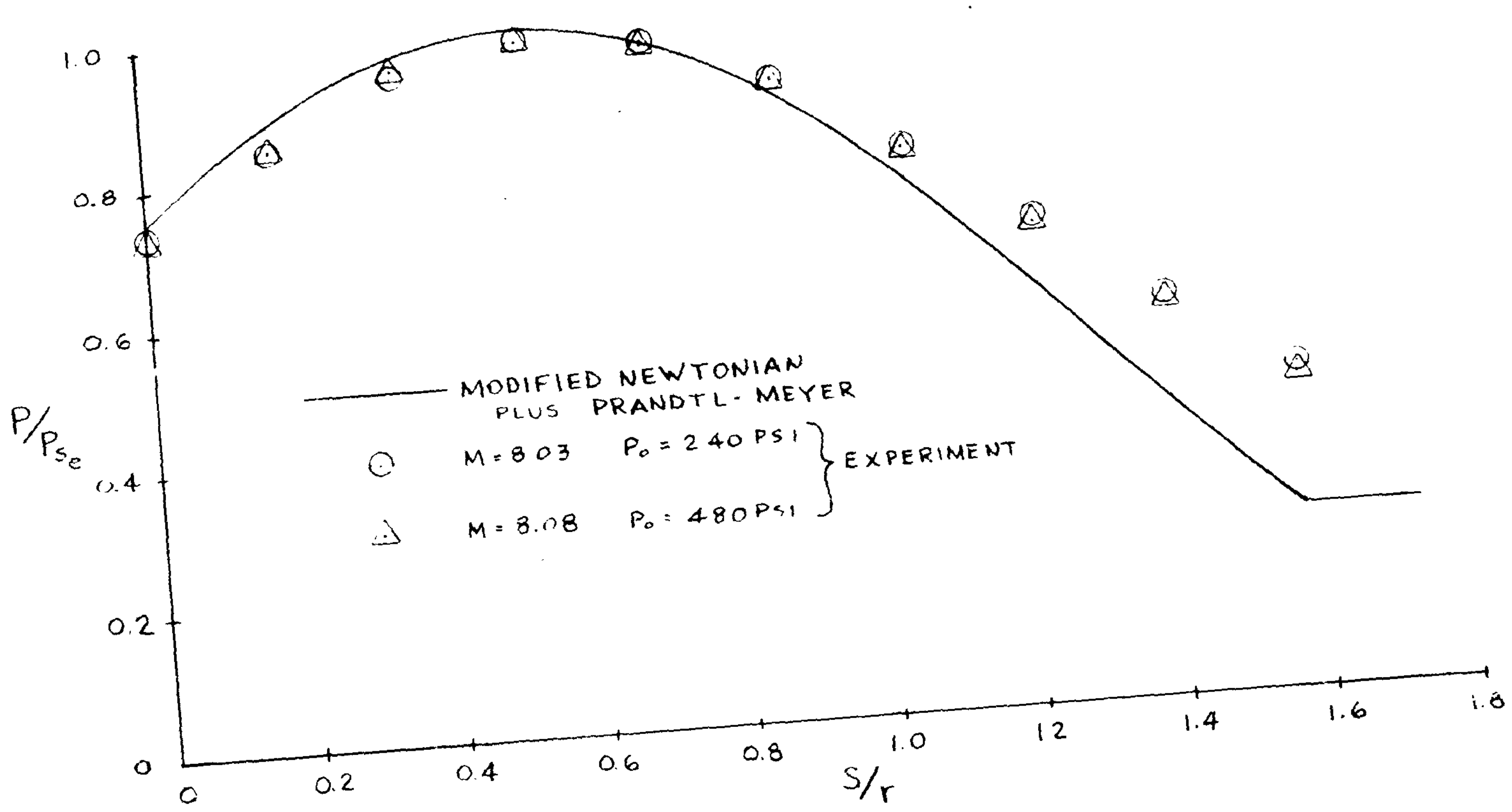

Figure 11 - Pressure Distribution on the Nose Cylinder of the 0.50 Inch Nose Radius Flat Plate Model - $\alpha = 30^\circ$

[redacted]

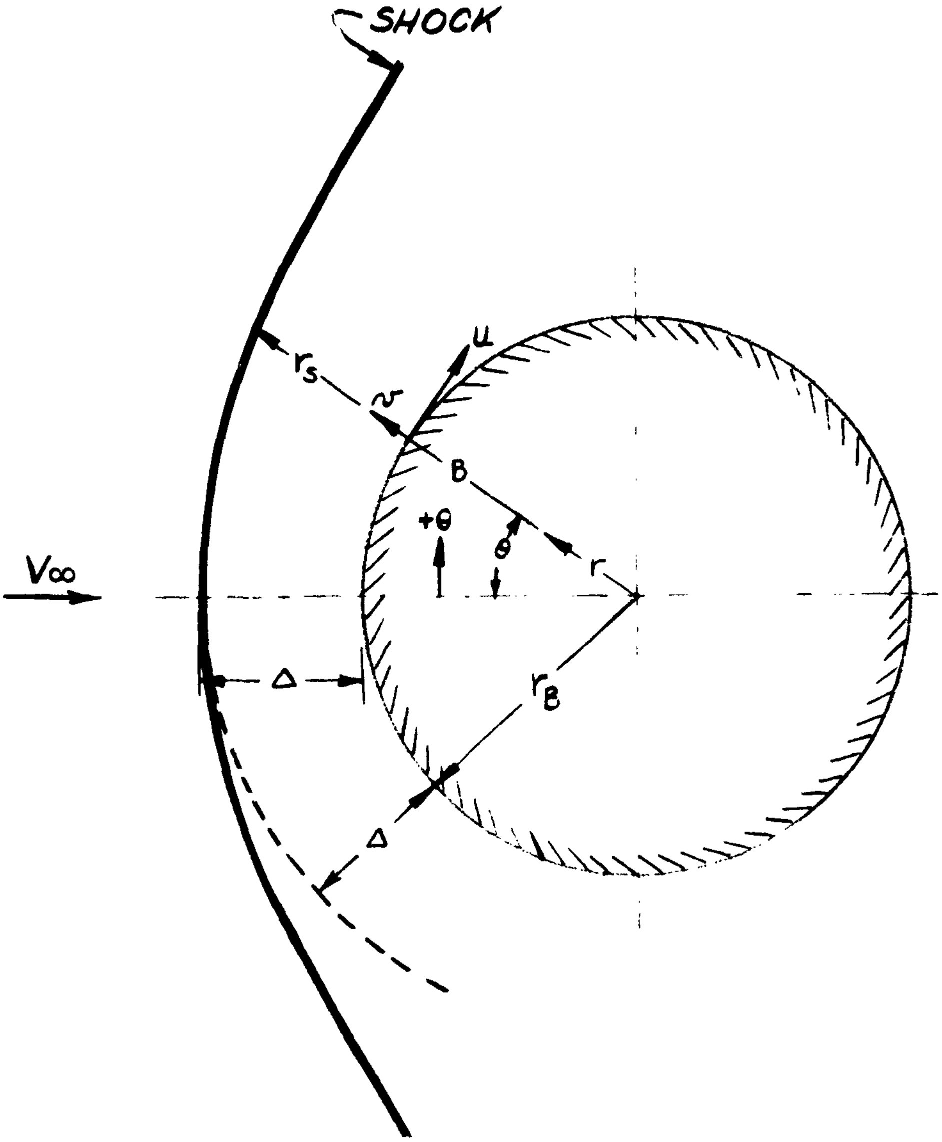

Figure 12 - Coordinate System for the Transonic Analysis

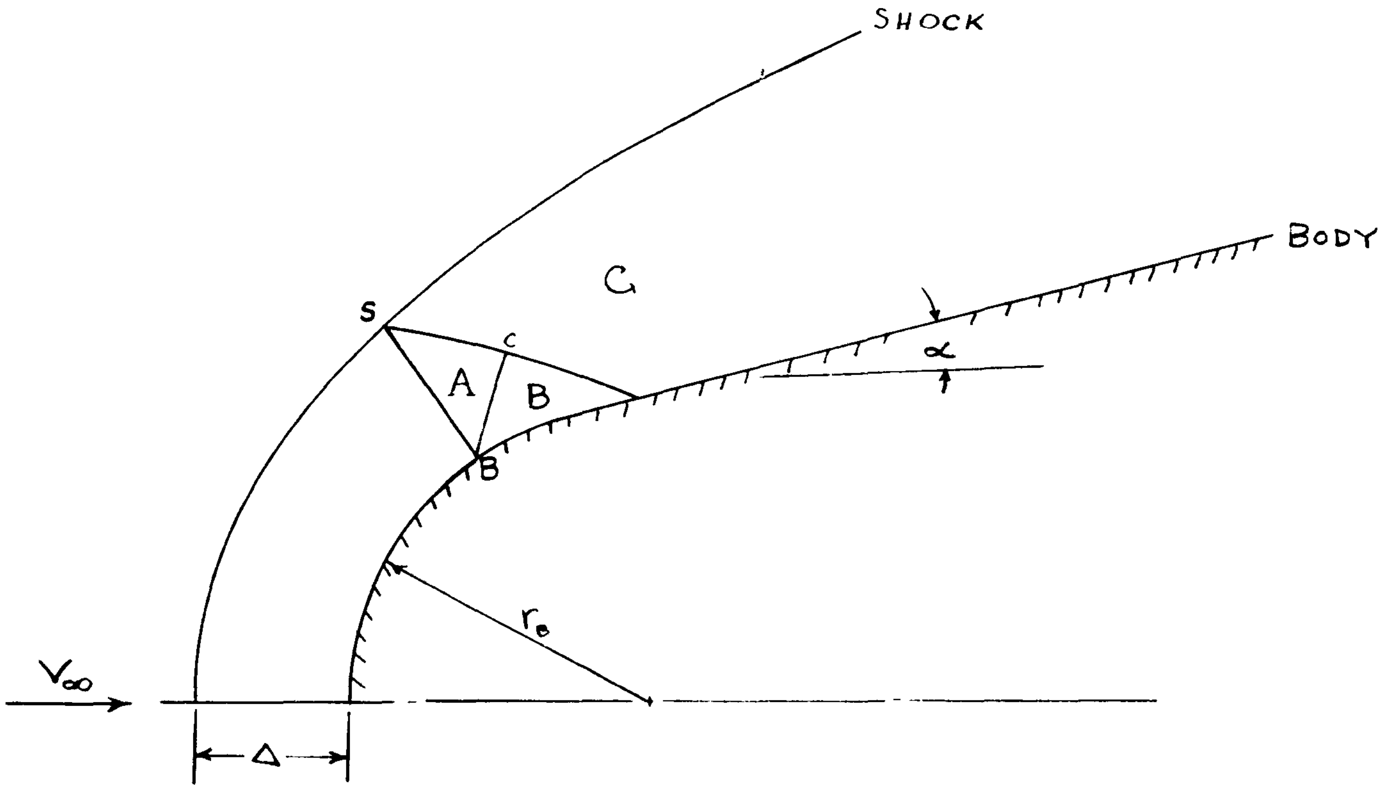

Figure 13 - Definition of Various Regions for the Characteristic Analysis

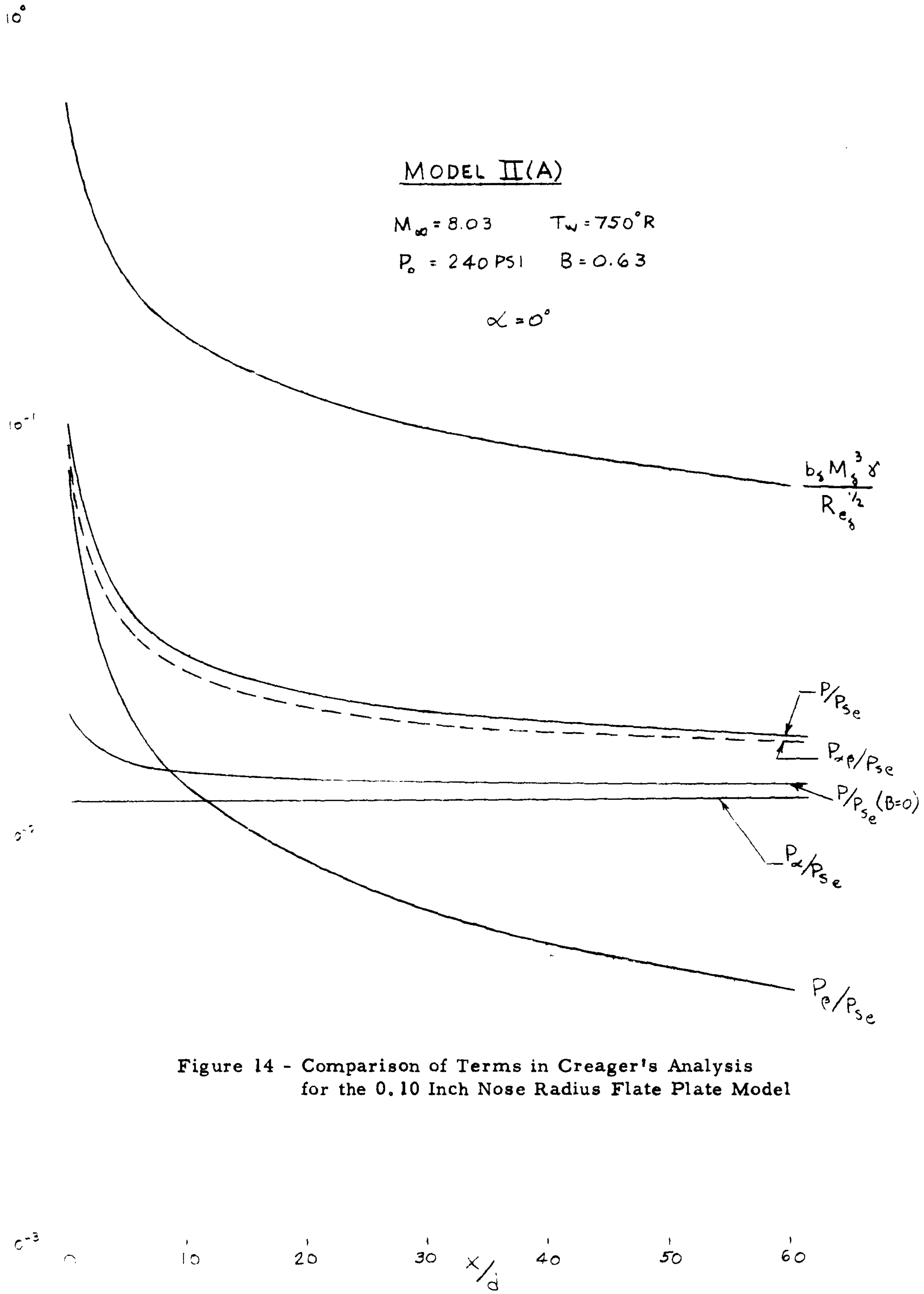

Figure 14 - Comparison of Terms in Creager's Analysis for the 0.10 Inch Nose Radius Flate Plate Model

Figure 15 - Comparison of Terms in Creager's Analysis for the 0.50 Inch Nose Radius Flat Plate Model.

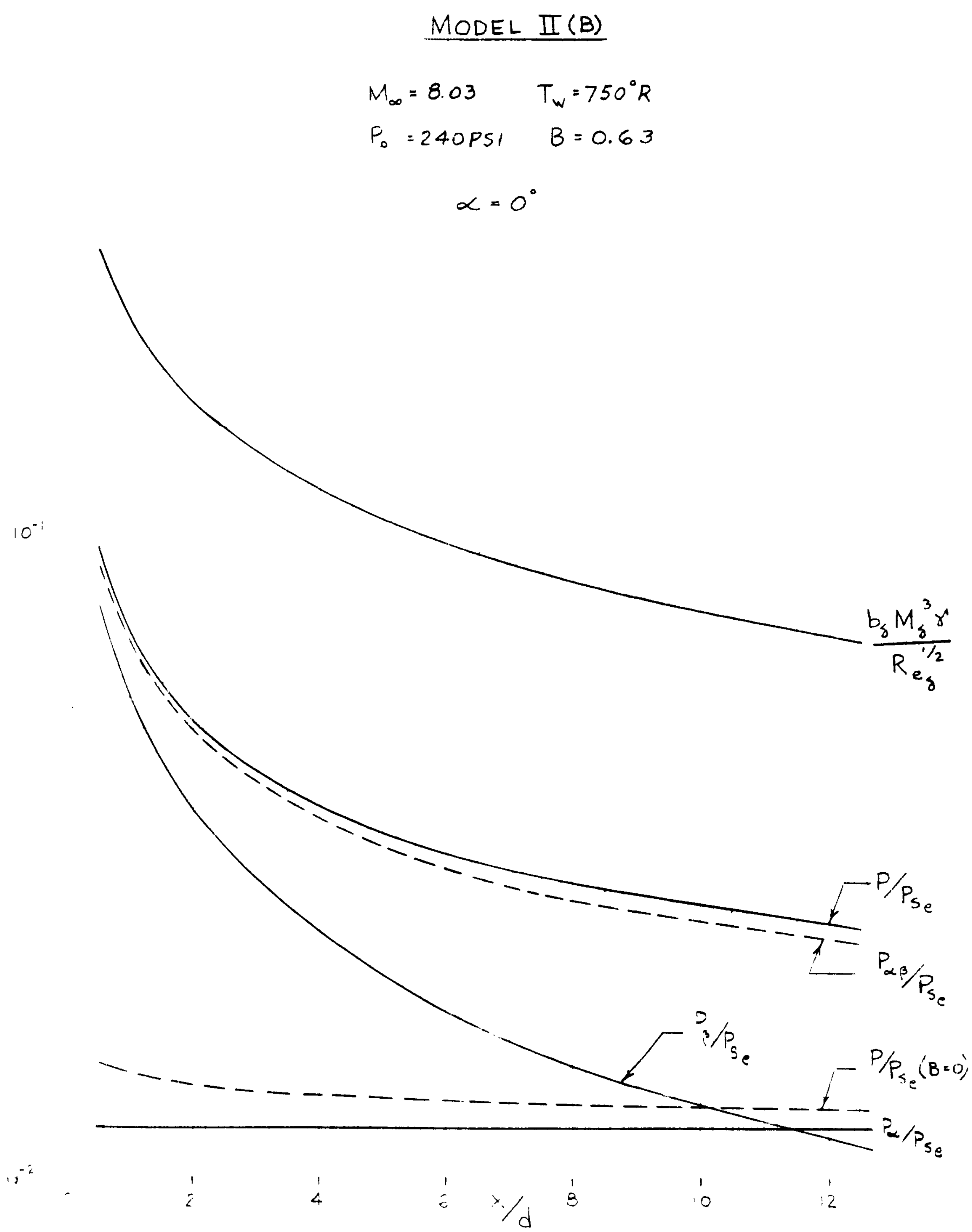

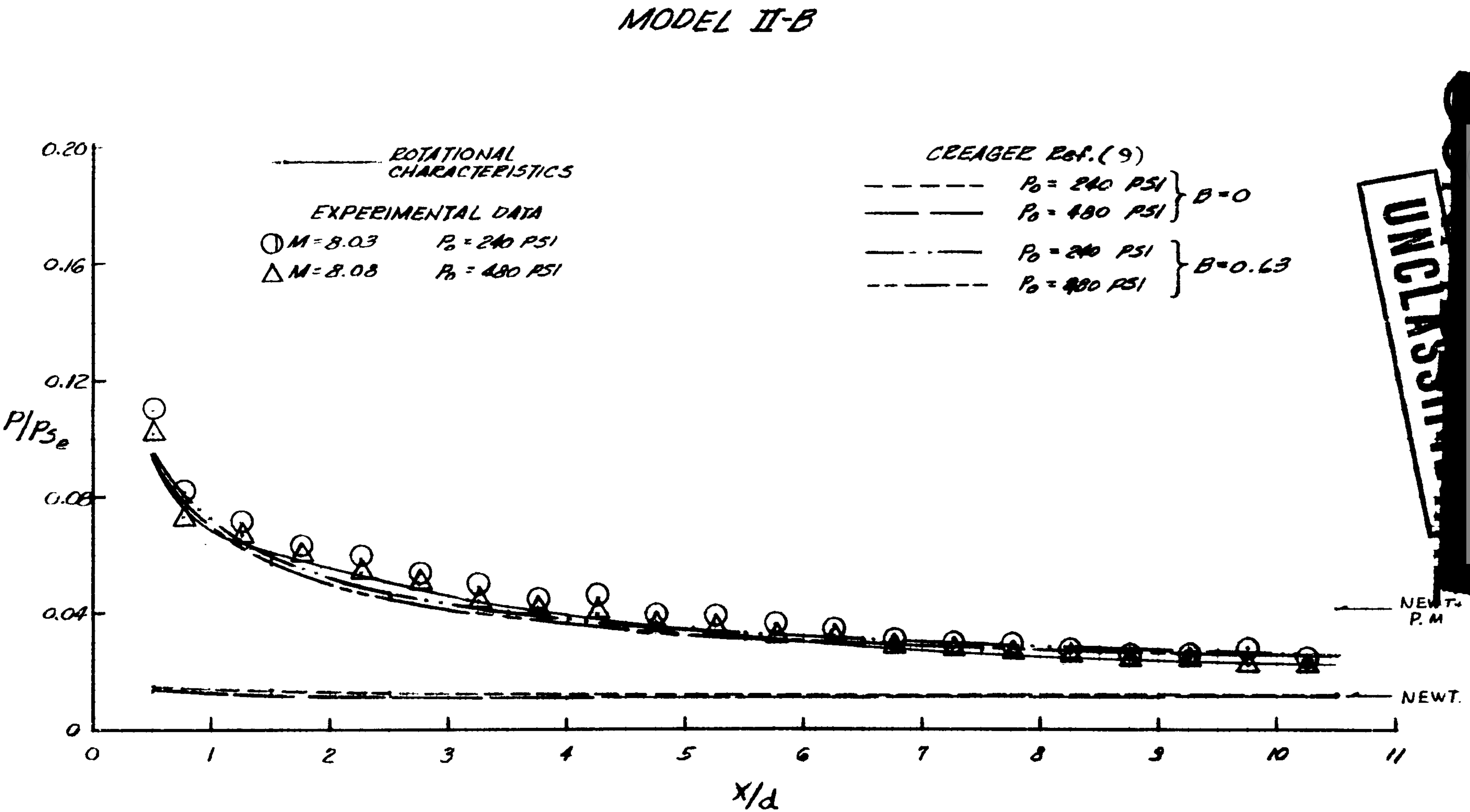

Figure 16 - Axial Pressure Distribution for the 0.50 Inch Nose Radius Flate Plate Model - $\alpha = 0^\circ$

[redacted]

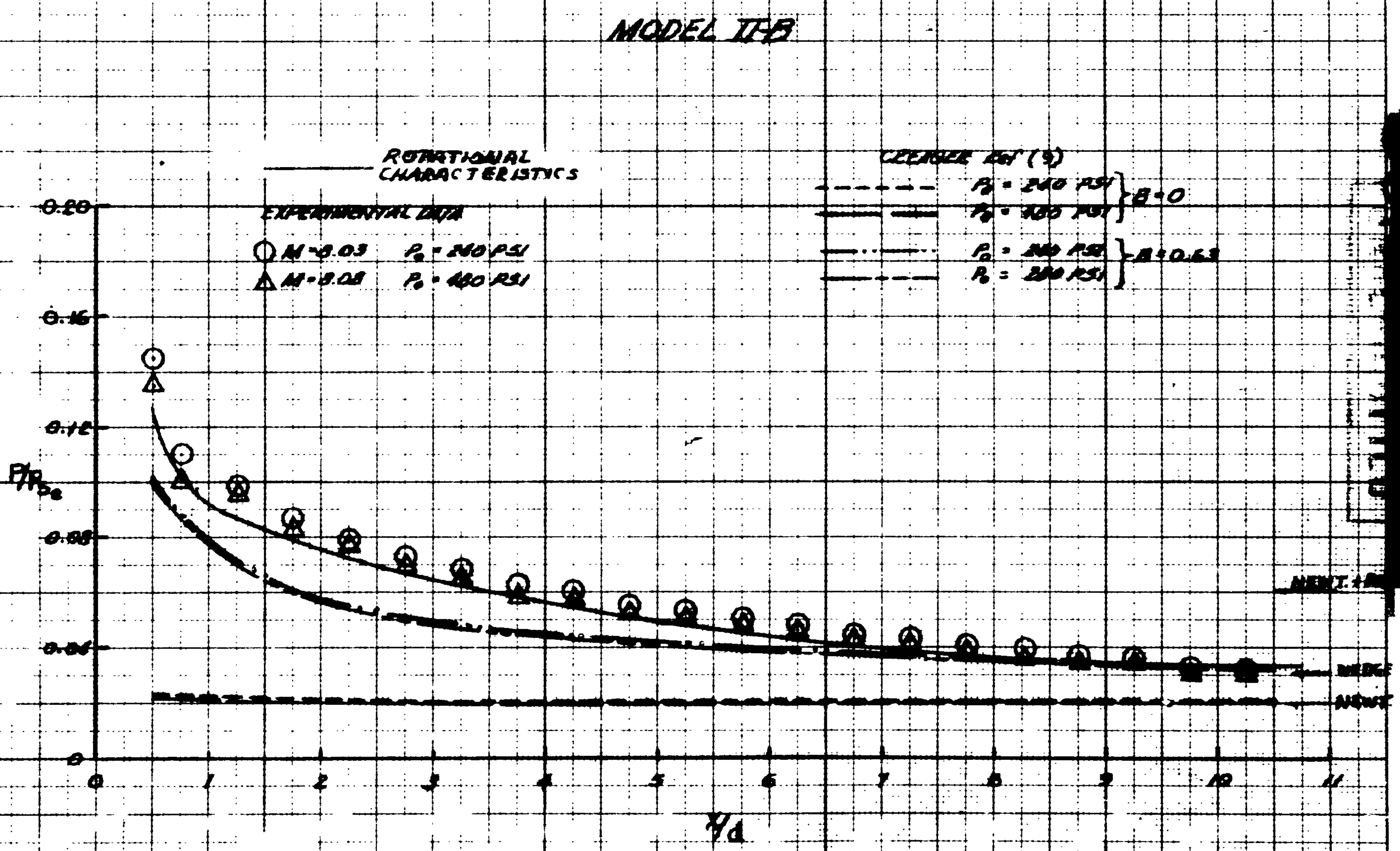

Figure 17 — Axial Pressure Distribution for the 0.50 Inch Nose Radius Flat Plate Model - α = 5°

[redacted]

[redacted]

[redacted]

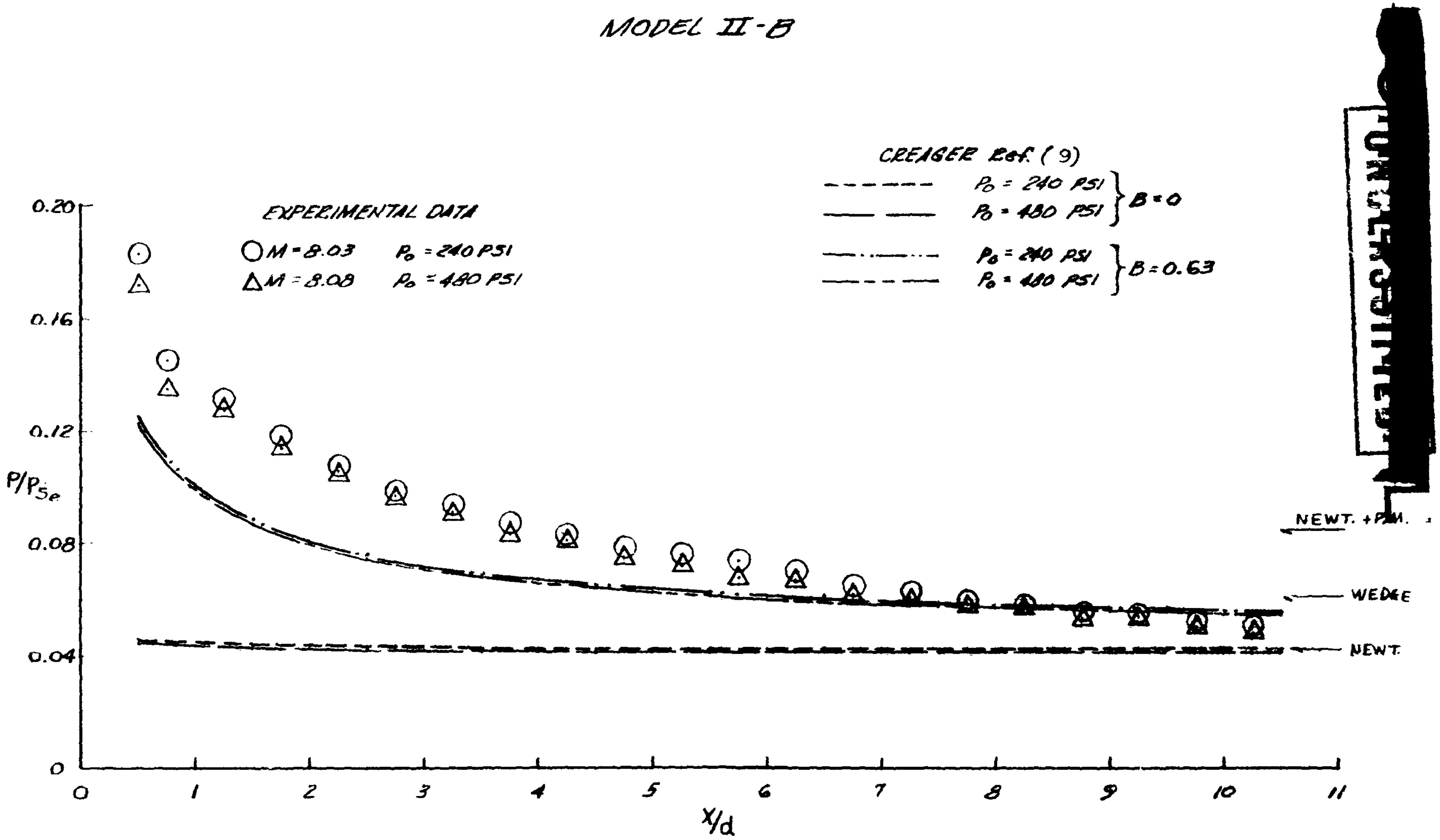

Figure 18 - Axial Pressure Distribution for the 0.50 Inch Nose Radius Flat Plate Model - $\alpha = 10°$

UNCLASSIFIED

[redacted]

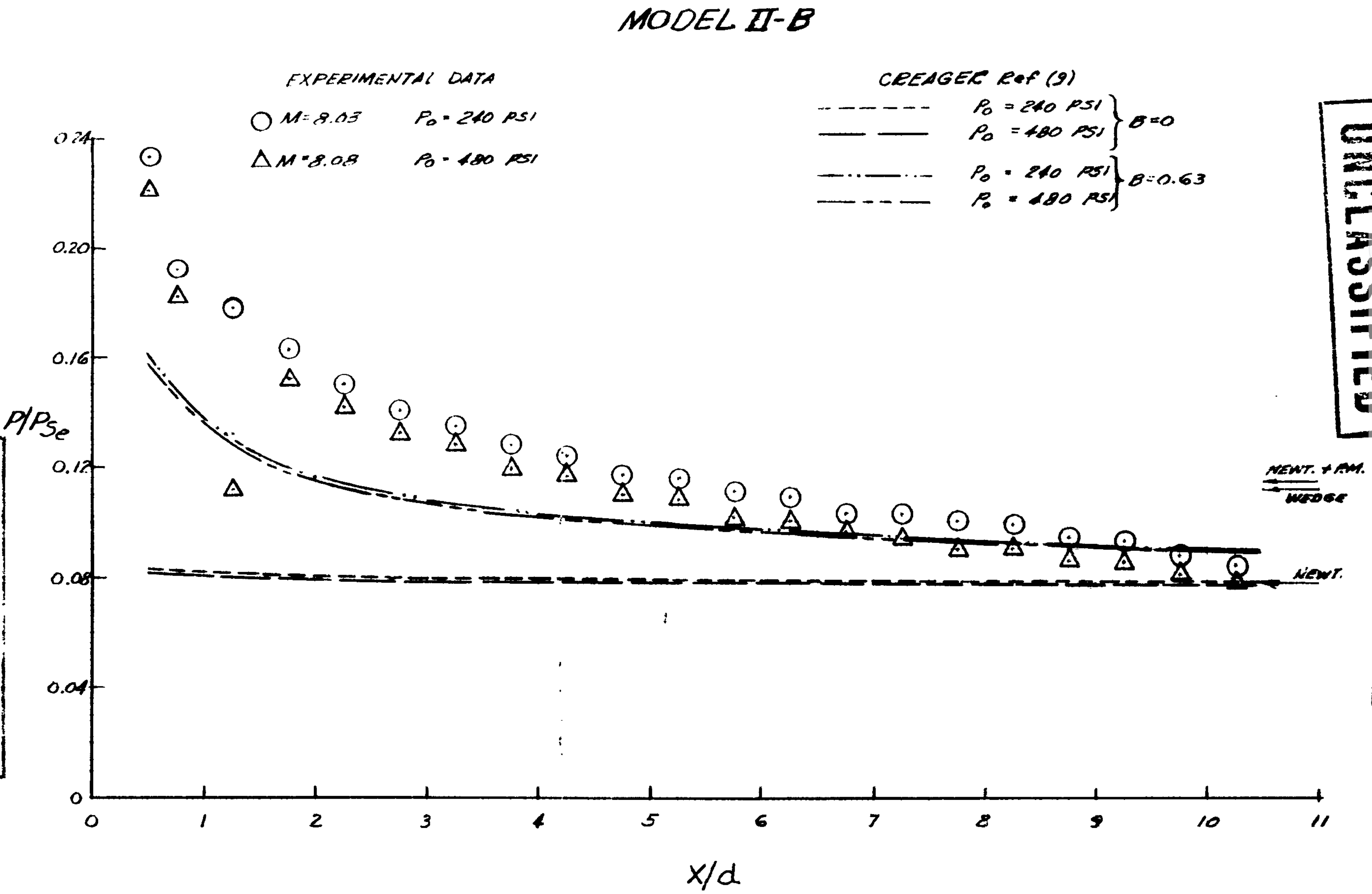

Figure 19 - Axial Pressure Distribution for the 0.50 Inch Nose Radius Flat Plate Model - α = 15°

[redacted]

[redacted]

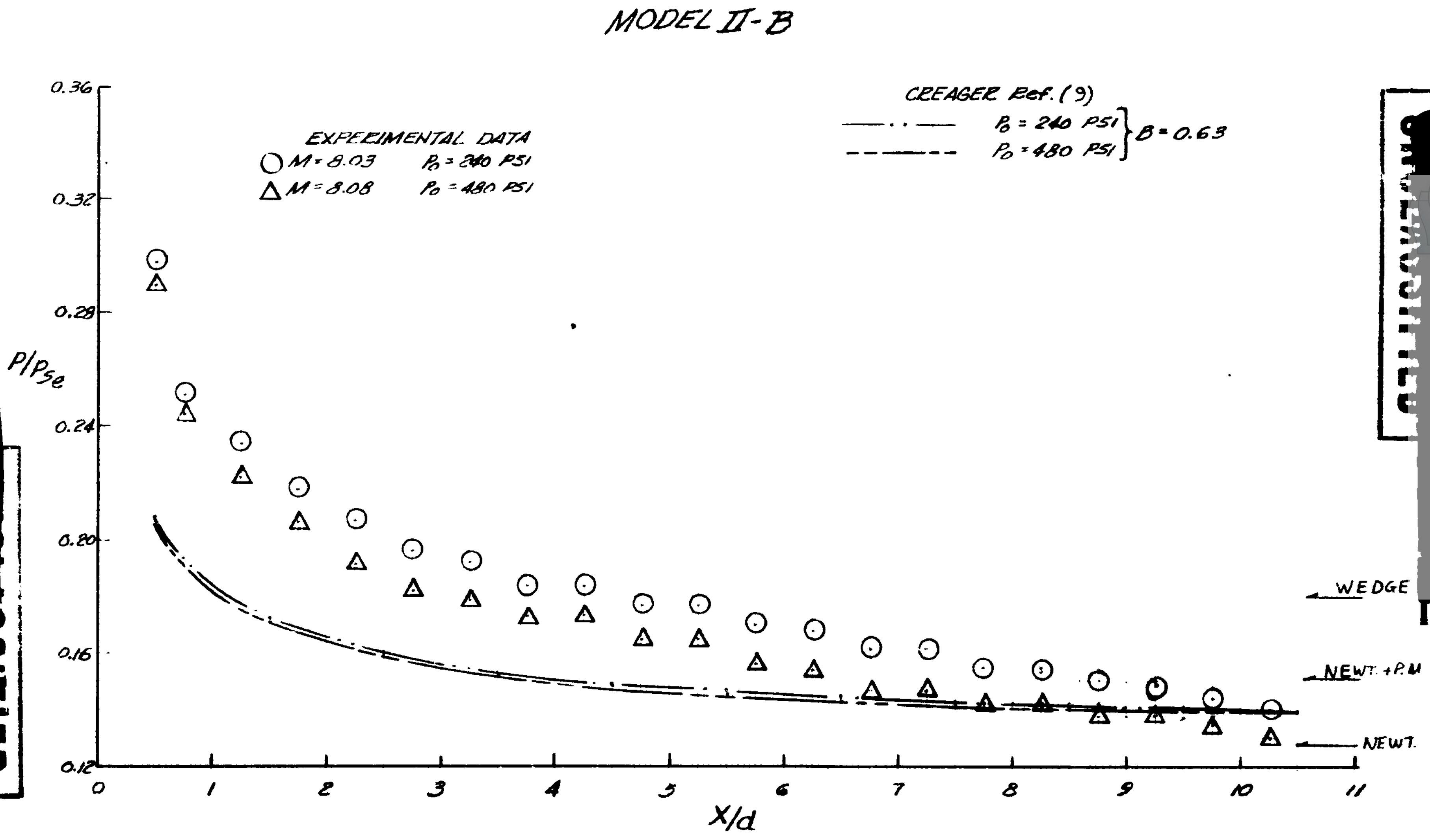

Figure 20 - Axial Pressure Distribution for the 0.50 Inch Nose Radius Flat Plate Model - α = 20°

[redacted]

UNCLASSIFIED

[redacted]

[redacted]

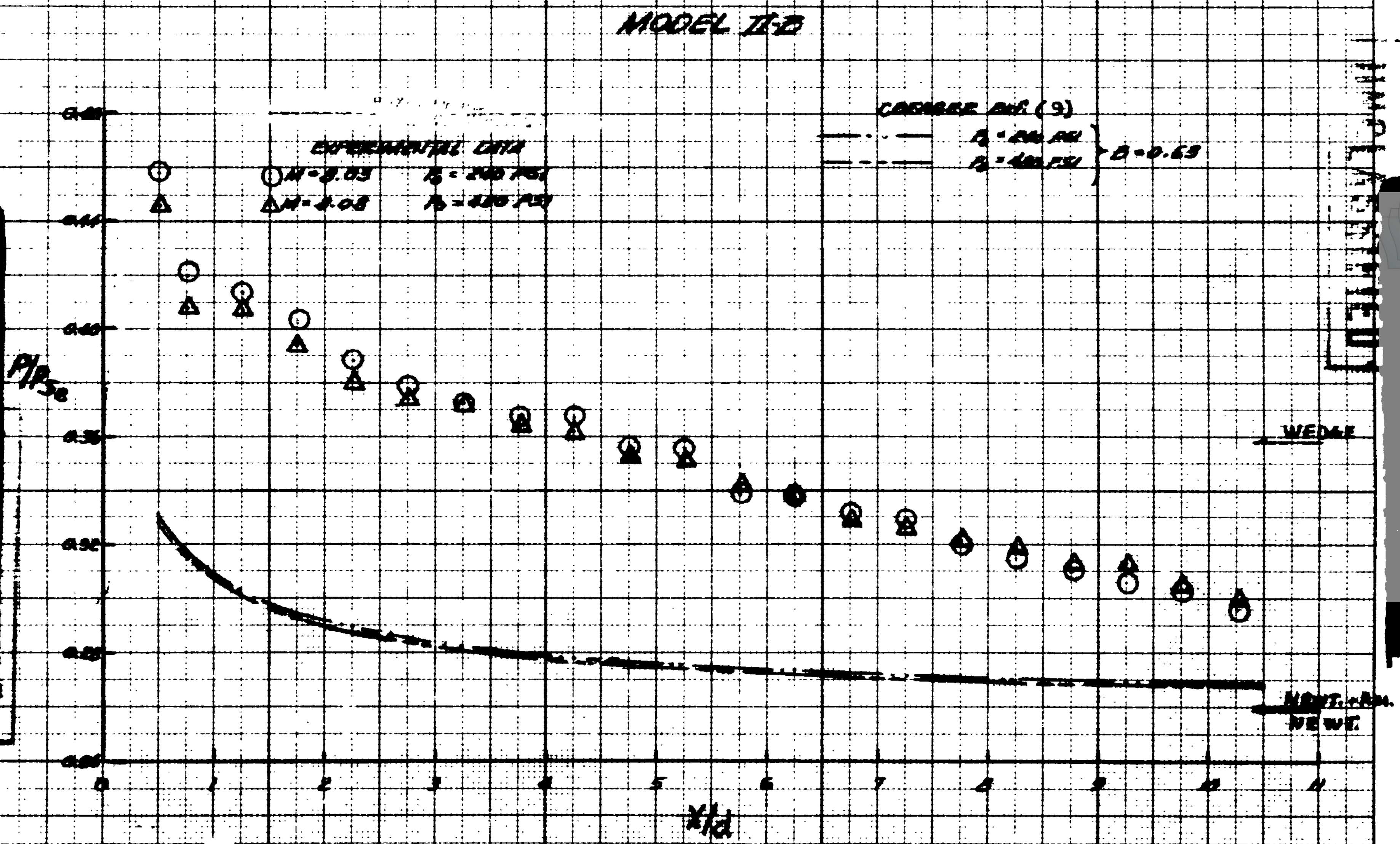

Figure 21 - Axial Pressure Distribution for the 0.50 Inch Nose Radius Flat Plate Model, $\alpha_c = 30^\circ$

[redacted]

[redacted]

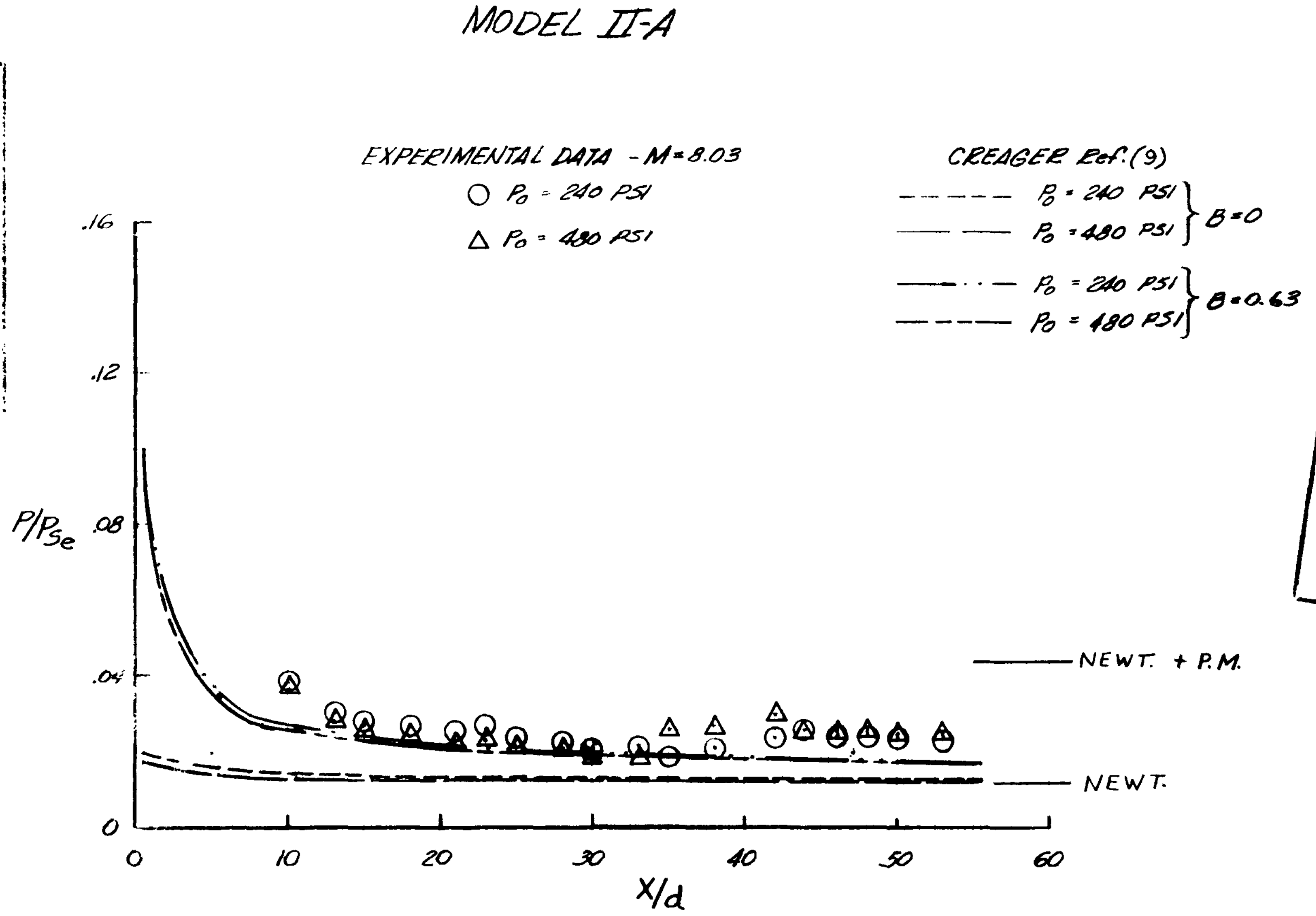

Figure 22 - Axial Pressure Distribution on the 0.10 Inch Nose Radius Flat Plate Model - $\alpha = 0^o$

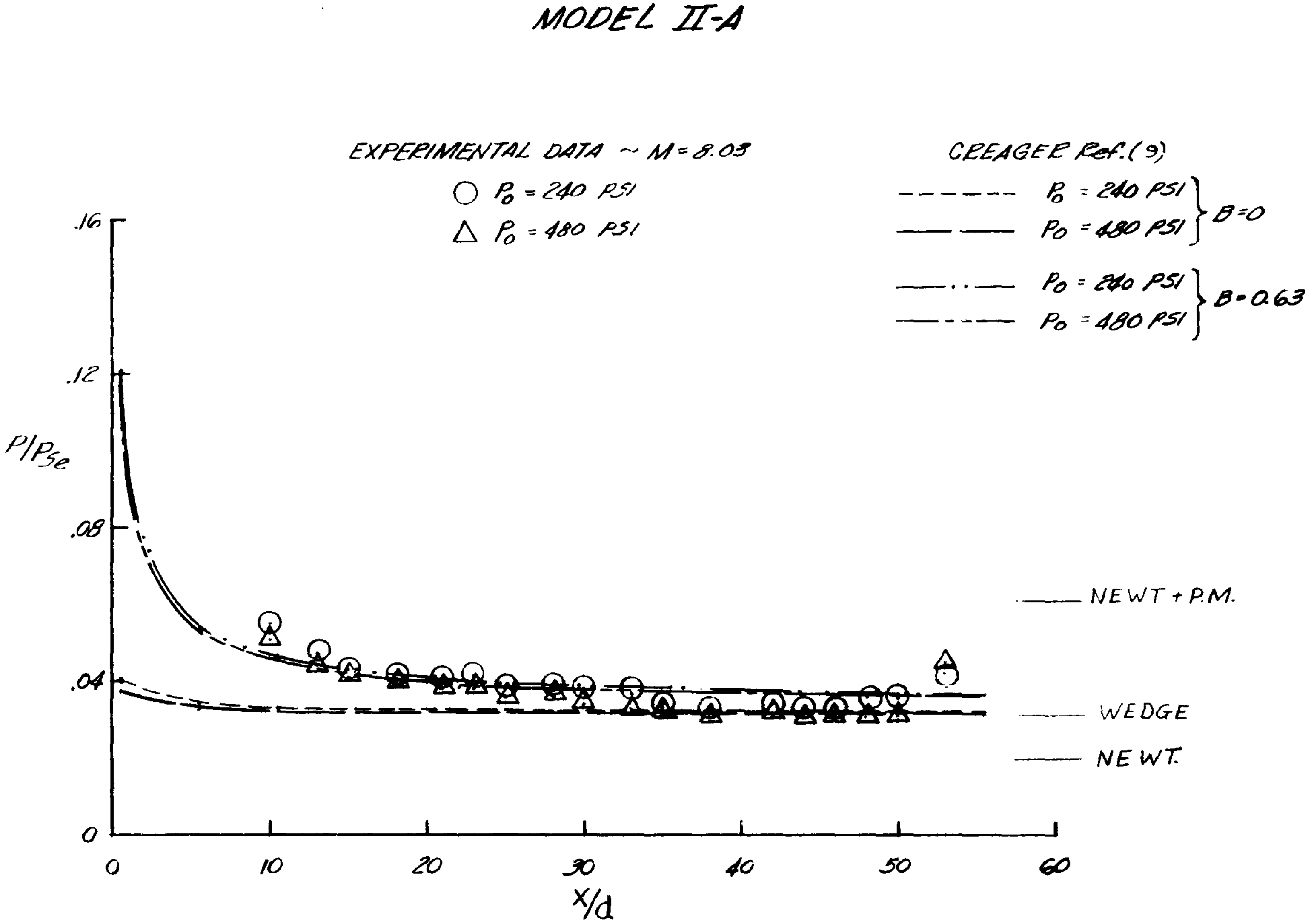

Figure 23 - Axial Pressure Distribution on the 0.10 Inch Nose Radius Flat Plate Model - $\alpha = 5^{\circ}$

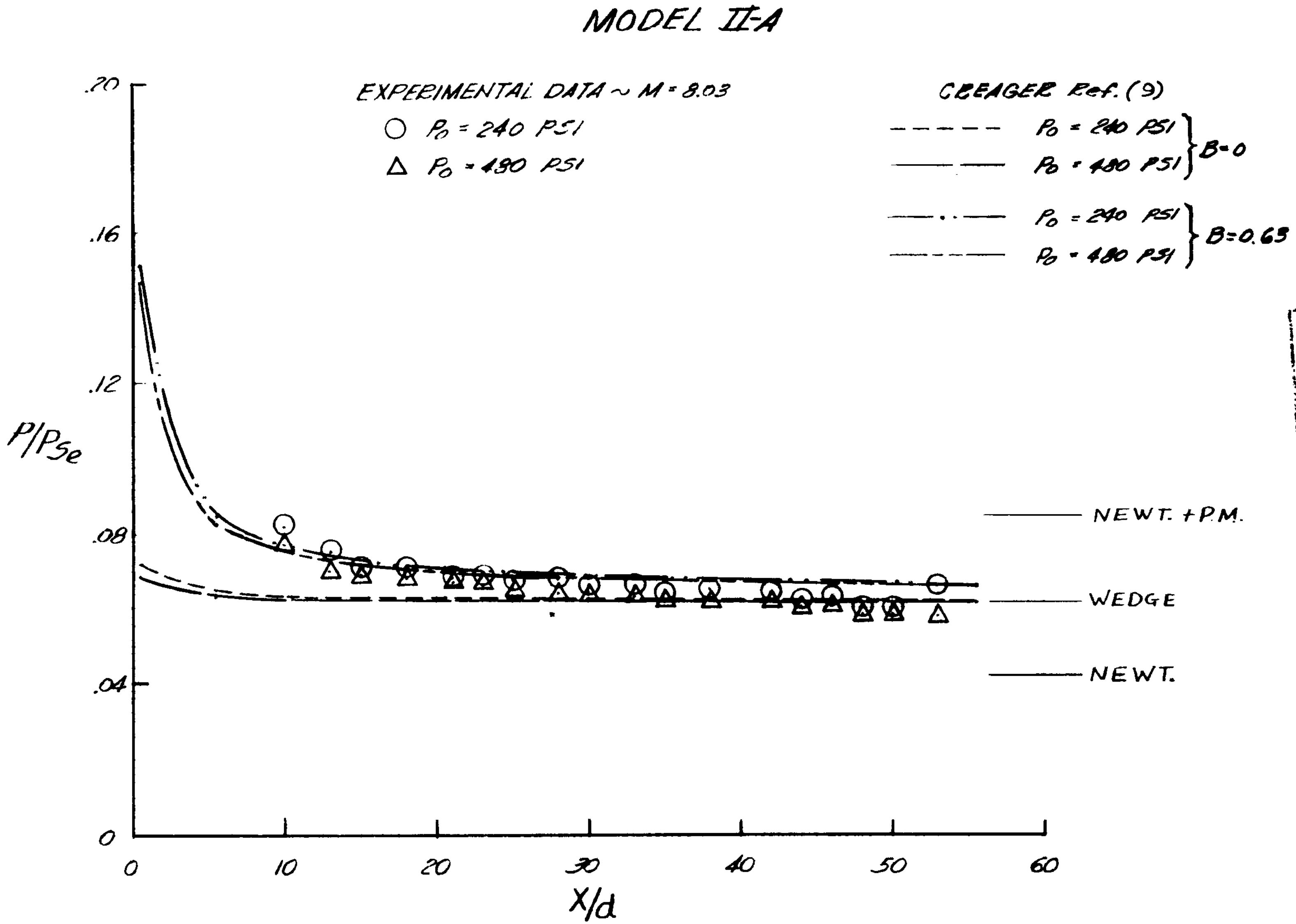

Figure 24 - Axial Pressure Distribution on the 0.10 Inch Nose Radius Flat Plate Model - $\alpha = 10^\circ$

[redacted]

[redacted]

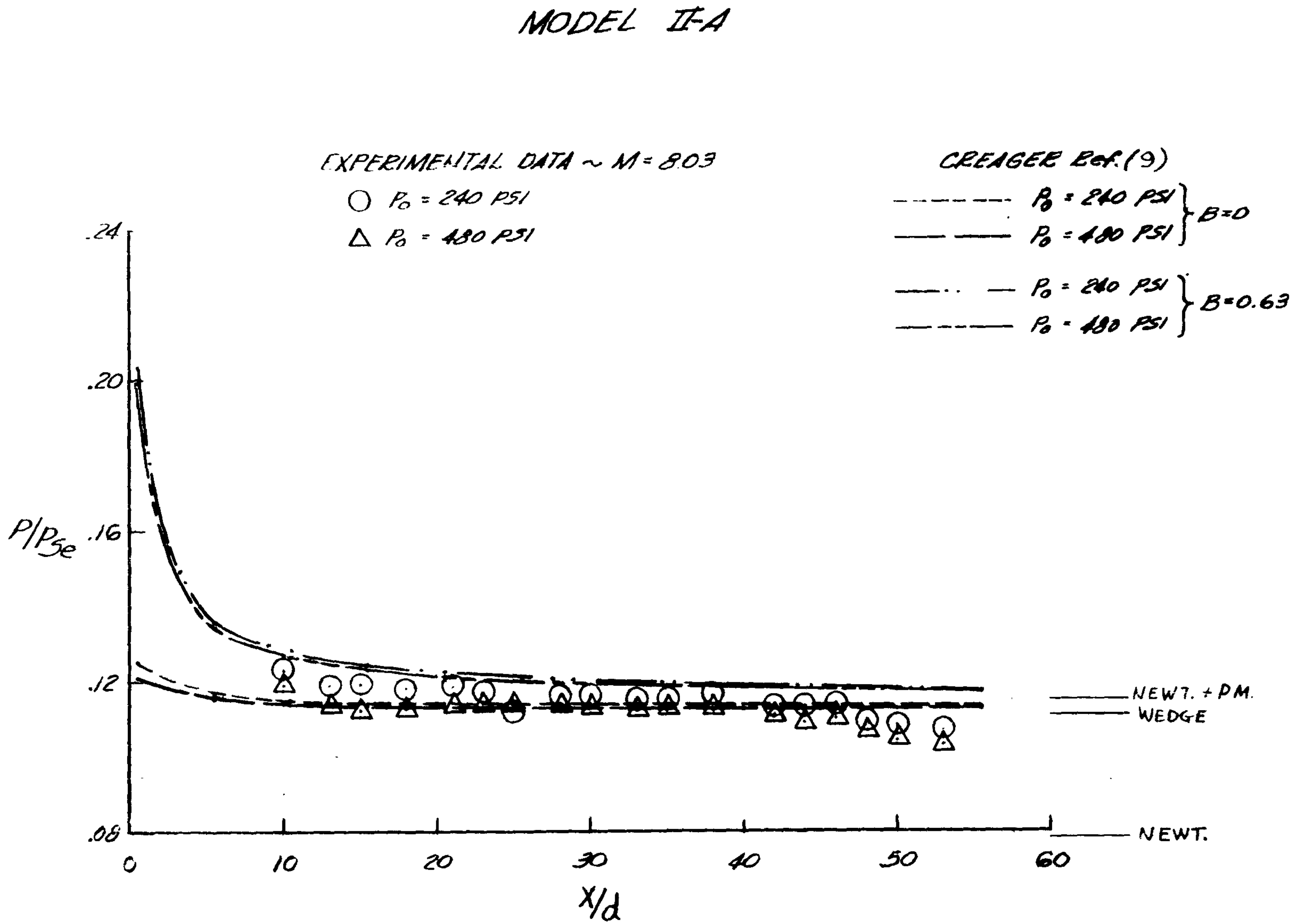

Figure 25 - Axial Pressure Distribution on the 0.10 Inch Nose Radius Flat Plate Model - α = 15°

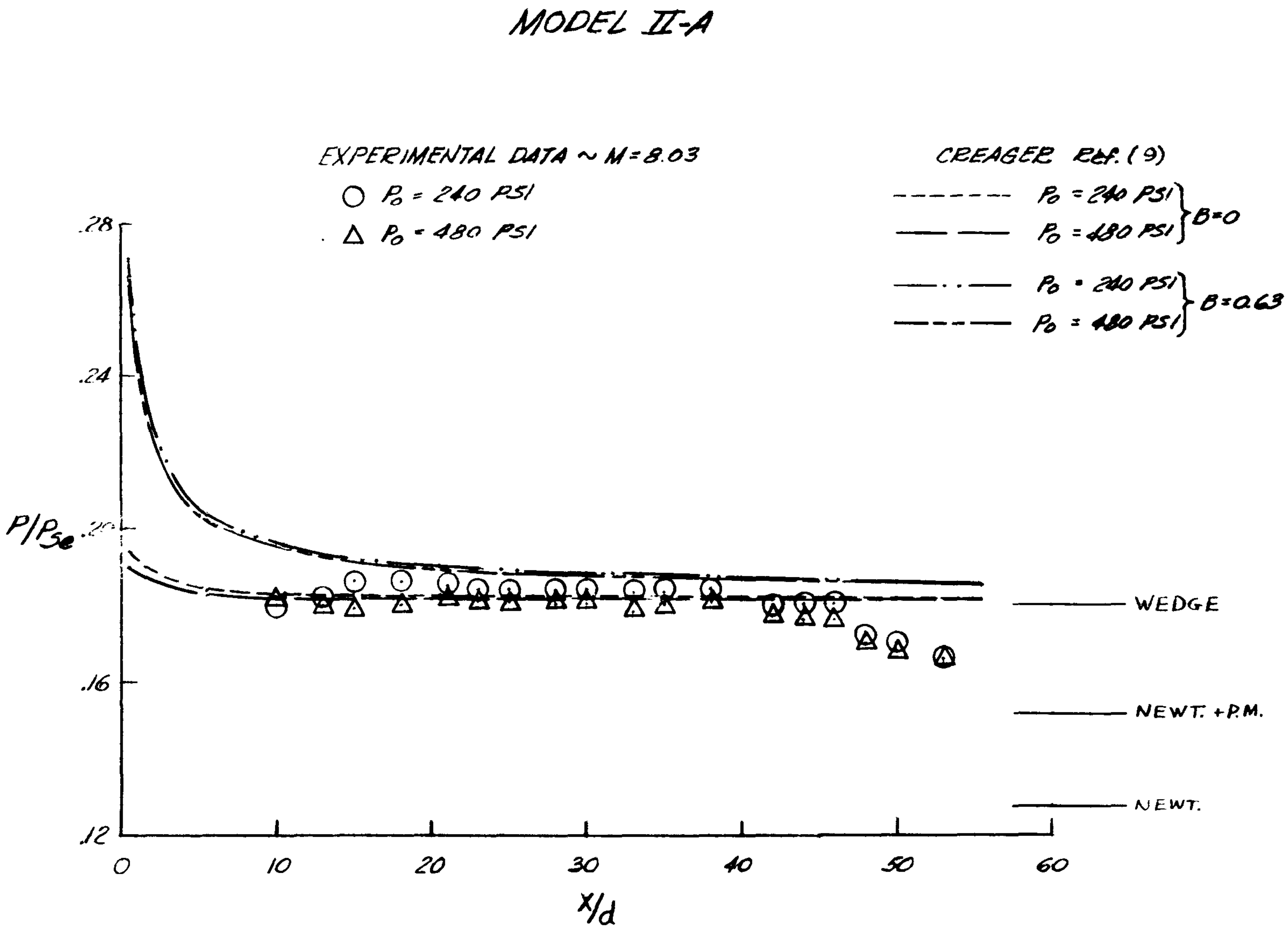

Figure 26 - Axial Pressure Distribution on the 0.10 Inch Nose Radius Flat Plate Model - α = 20°

[redacted]

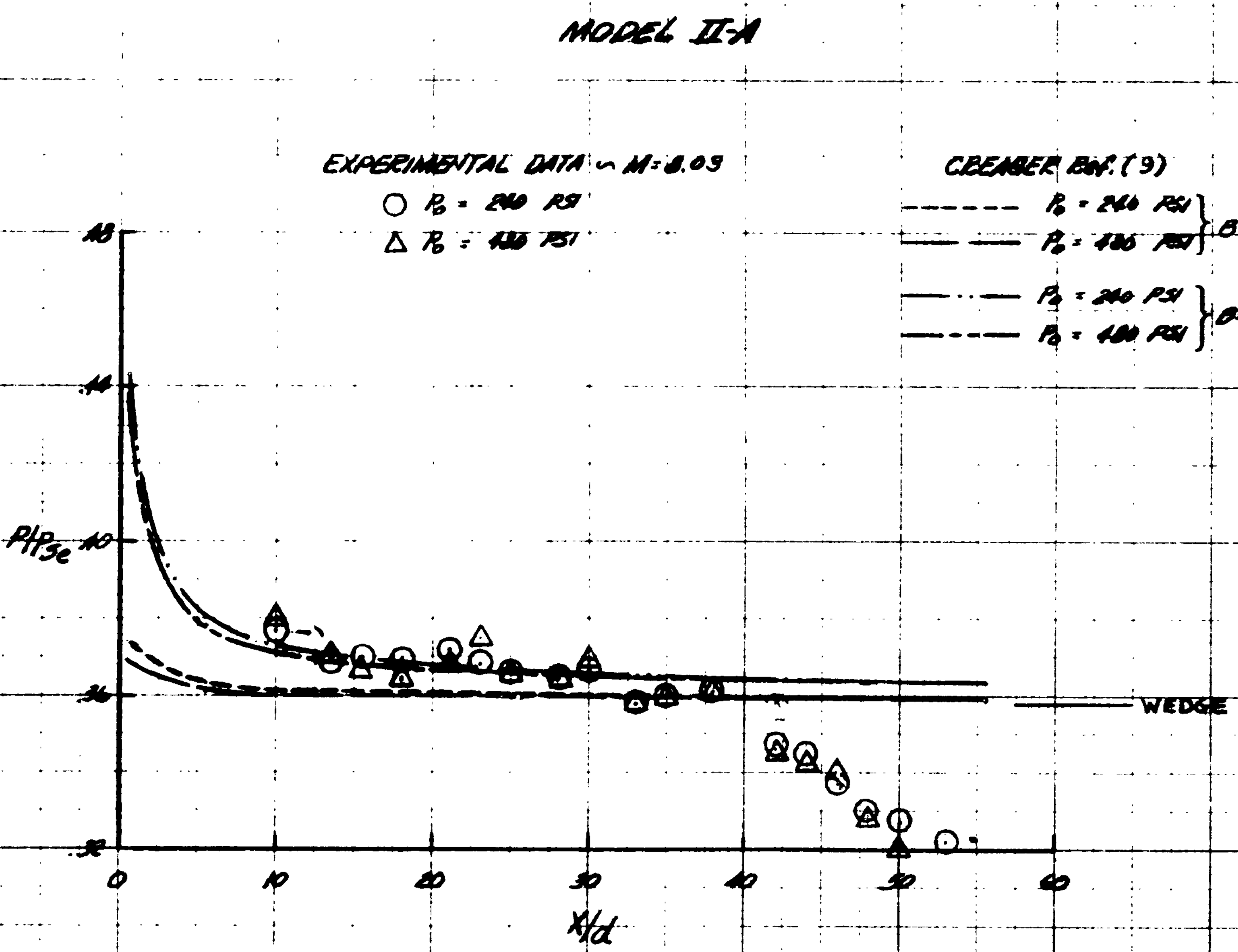

Figure 27 - Axial Pressure Distribution on the 0.10 Inch Nose Radius Flat Plate Model - α = 30°

[redacted]

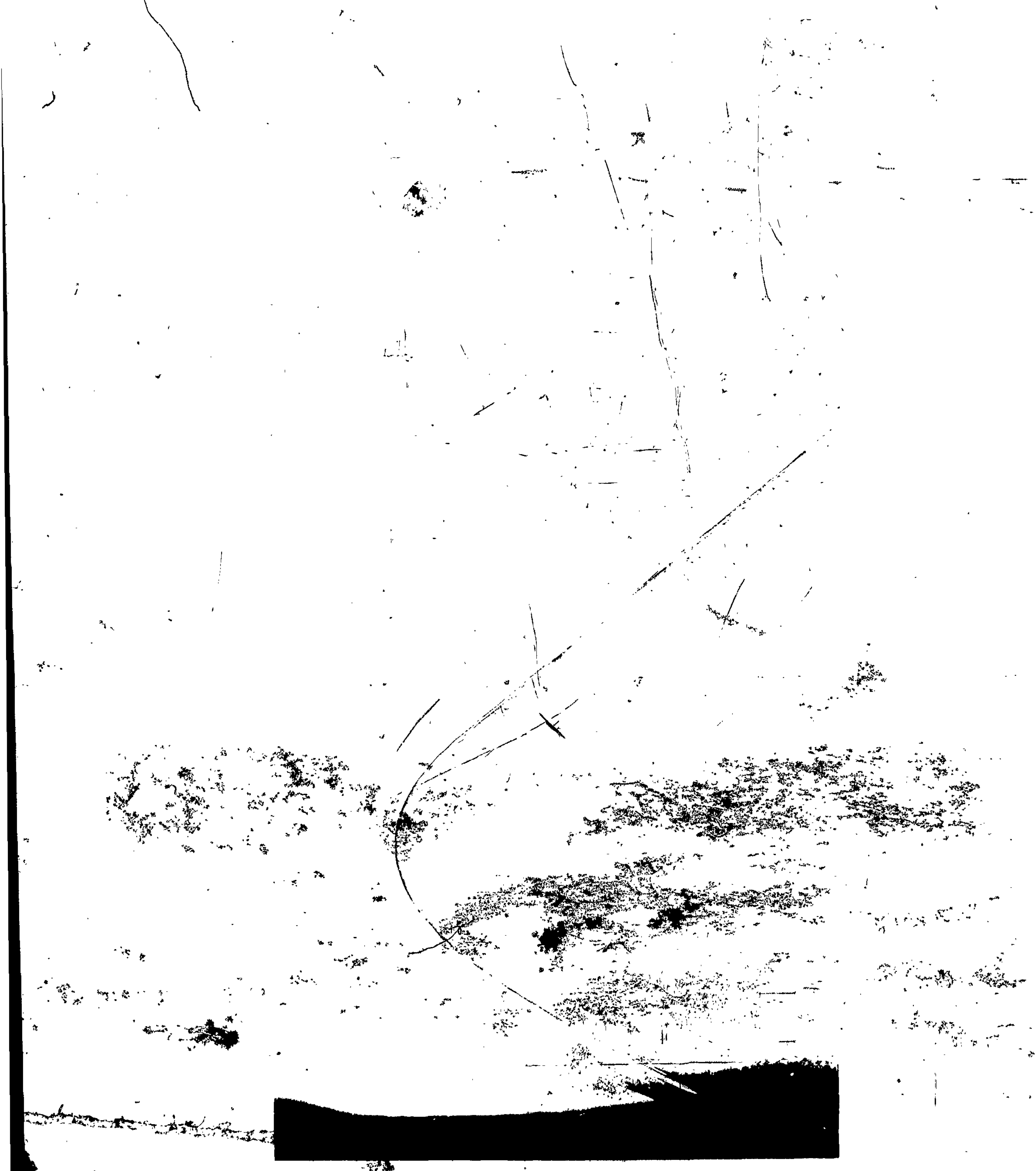

Figure 28 - Shadowgraph of the Flow Over the 0.50 Inch Nose Radius Flat Plate Model

Figure 29 - Shadowgraph of the Flow Over the 0.50 Inch Nose Radius Flat Plate Model

Figure 30 - Shadowgraph of the Flow Over the 0.50 Inch Nose Radius Flat Plate Model

Figure 31 - Shadowgraph of the Flow Over the 0.50 Inch Nose Radius Flat Plate Model

Figure 32 - Shadowgraph of the Flow Over the 0.50 Inch Nose Radius Flat Plate Model

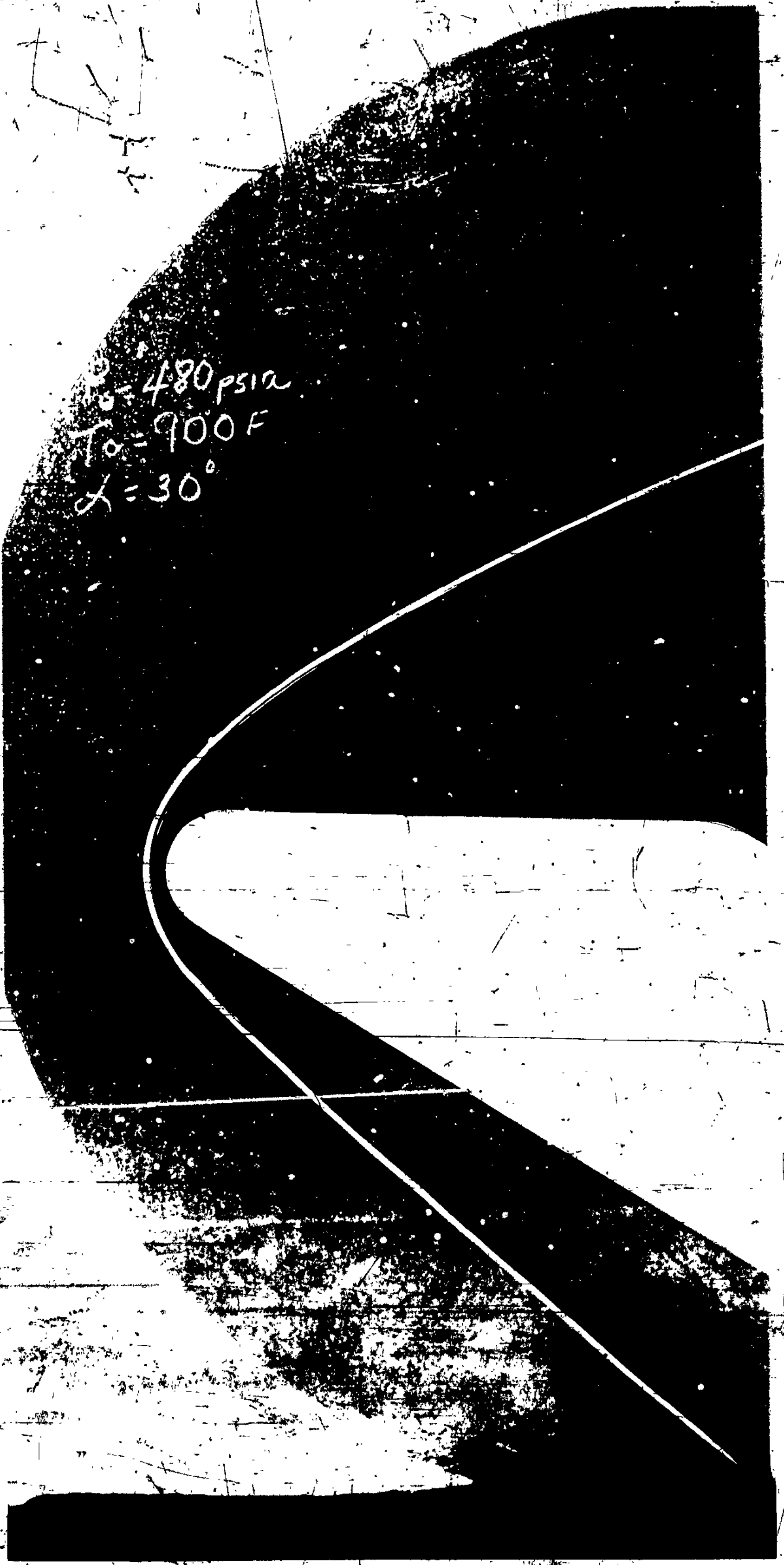

Figure 33 - Shadowgraph of the Flow Over the 0.50 Inch Nose Radius Flat Plate Model

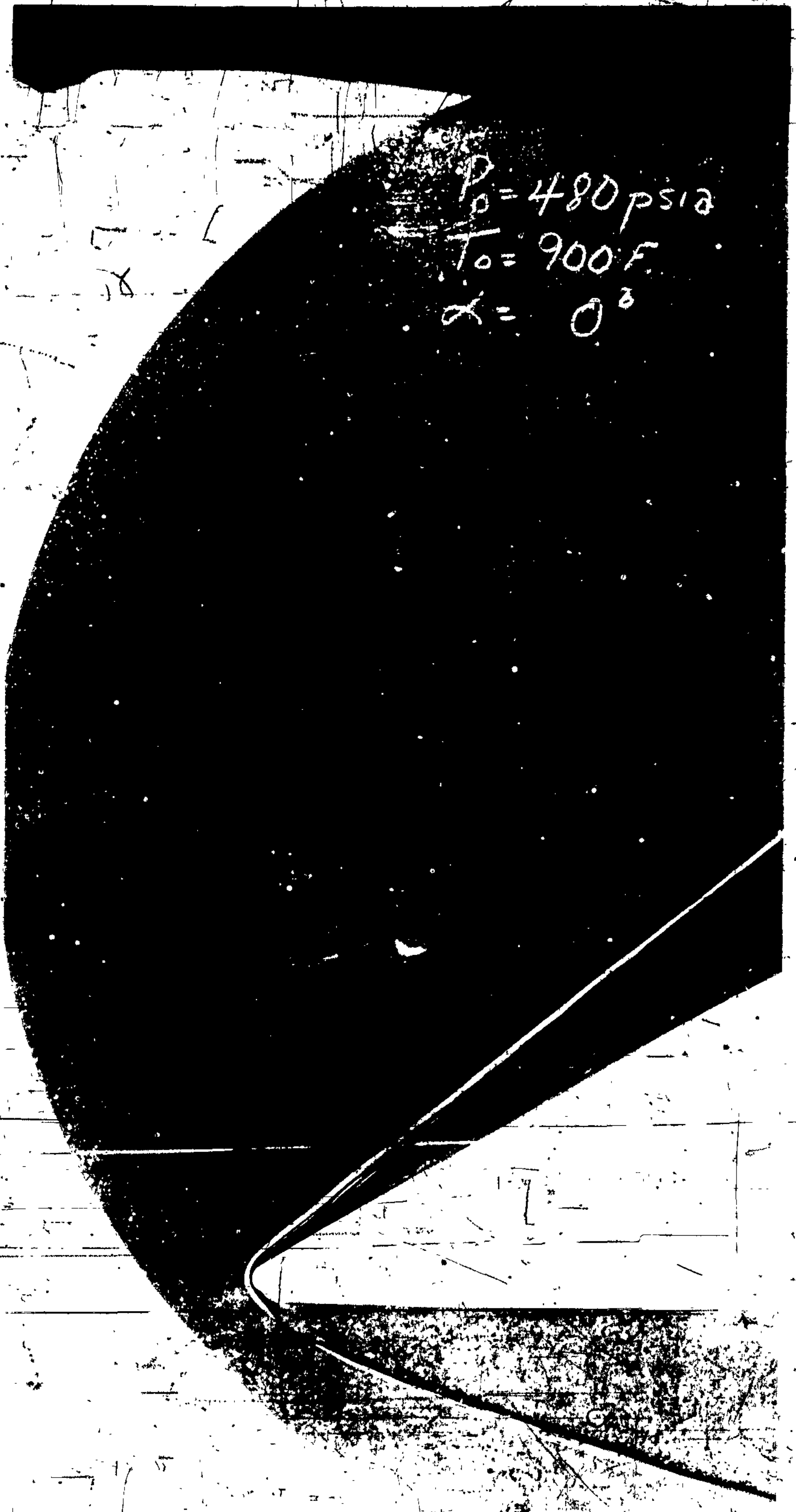

Figure 34 - Shadowgraph of the Flow Over the 0.10 Inch Nose Radius Flat Plate Model

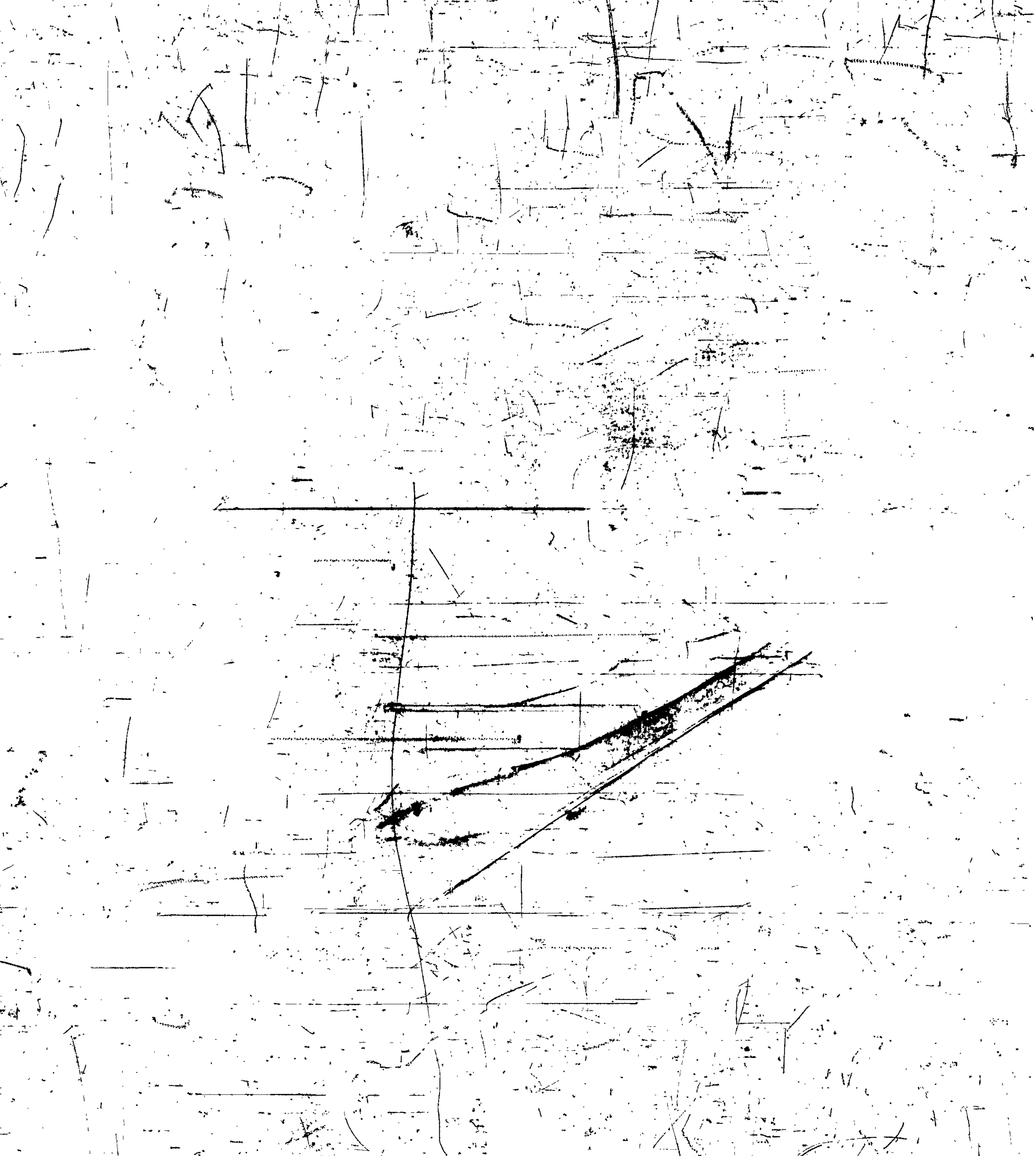

Figure 35 - Shadowgraph of the Flow Over the 0.10 Inch Nose Radius Flat Plate Model

Figure 36 - Shadowgraph of the Flow Over the 0.10 Inch Nose Radius Flat Plate Model

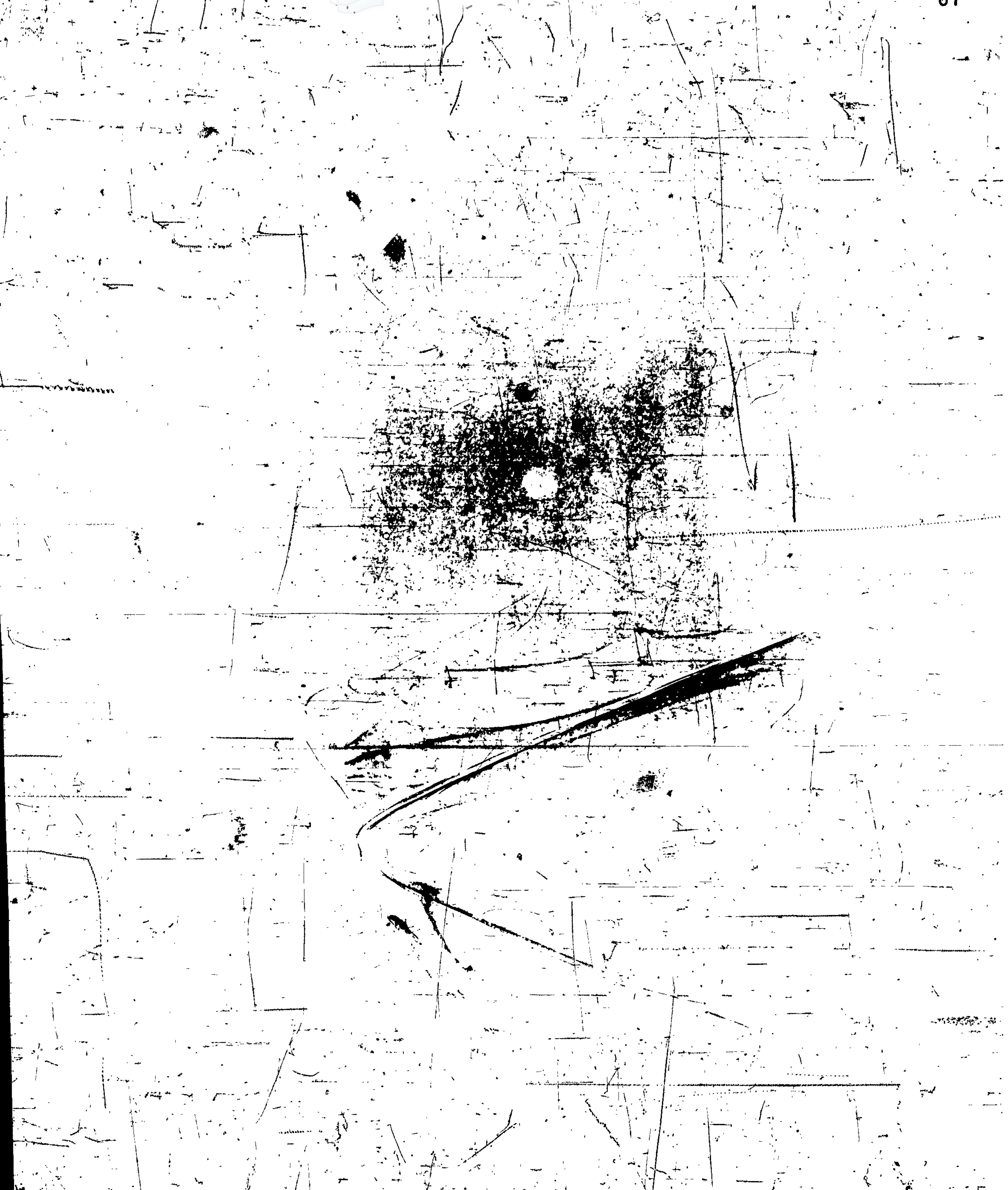

Figure 37 - Shadowgraph of the Flow Over the 0.10 Inch Nose Radius Flat Plate Model

Figure 38 - Shadowgraph of the Flow Over the 0.10 Inch Nose Radius Flat Plate Model

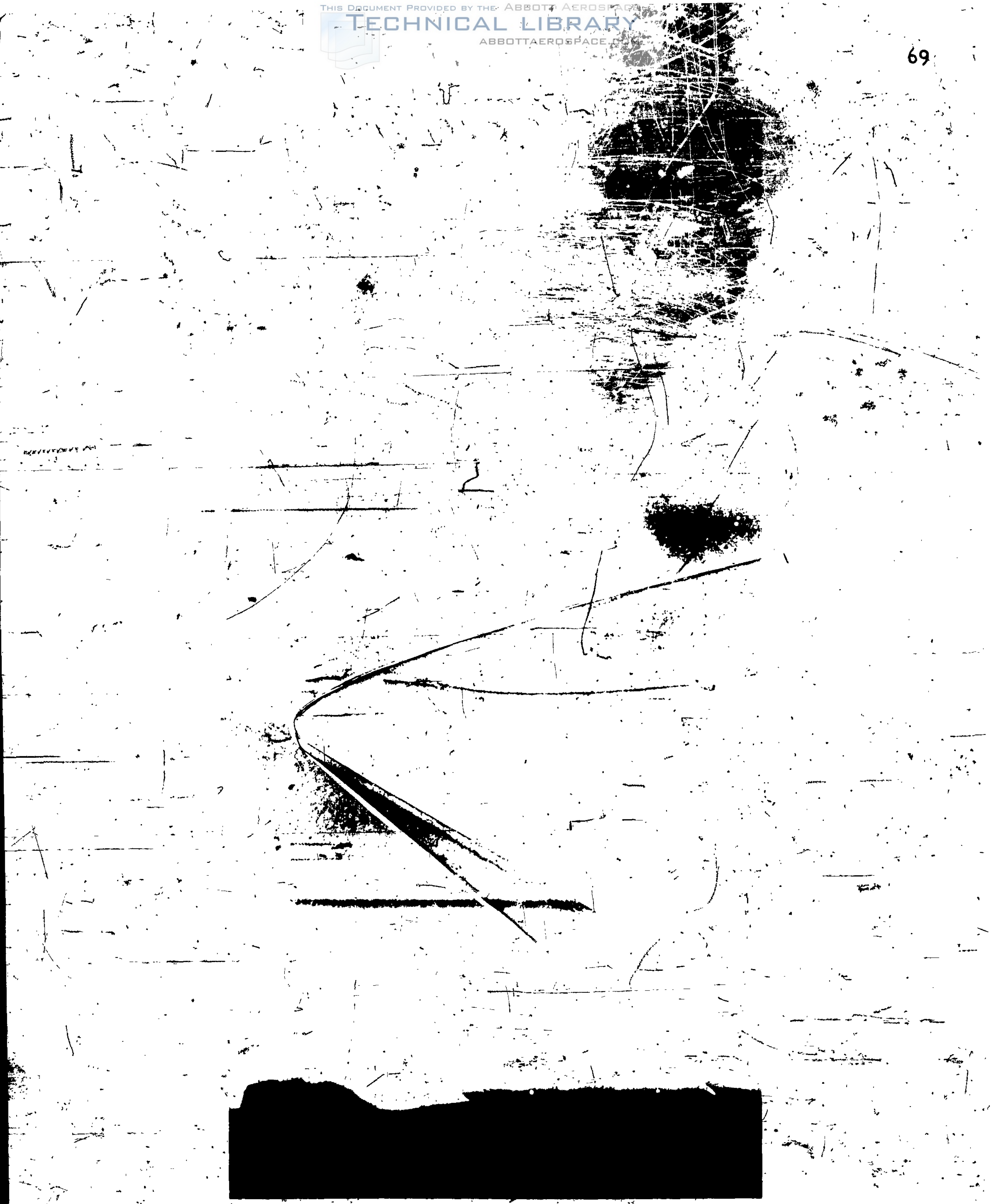

Figure 39 - Shadowgraph of the Flow Over the 0.10 Inch Nose Radius Flat Plate Model